Reviewer 1

We thank the reviewer for his time to carefully read the manuscript. However, we would like to clarify a few points.

It is important to state upfront that the integration of a 94-GHz FMCW radar on the Polar 5 is not the result of careful design for the aircraft selection (otherwise a higher altitude platform could have been selected) or the radar selection (where a single antenna, pulsed 94-GHz radar makes more sense). The research team was provided with one platform option and one available system that was designed for ground-based observations. Fortunately, the Polar 5 aircraft is large enough to accommodate a bistatic radar system and we agree with the reviewer that a bistatic radar system is not generally preferred for aircraft deployment. The reviewer is certainly familiar with FMCW signal processing and appreciates the foresight of the research team to point the radar off-nadir by 25 degrees. As the reviewer points out, the surface echo side lobes are considerably reduced with this configuration.

Regarding the selection of an FMCW system, we would like to add that this particular radar system is not the first FMCW 94-GHz radar system. The Naval Postgraduate School (NPS) and Prosensing were operating a 94-GHz radar system on a twin otter for over a decade. One of the co-authors (Kollias) was involved in the analysis of the observations from this system and we agree that the surface echo affects significantly our ability to see weak targets. Solid state, high duty cycle transmitters are the future as it was clearly demonstrated with the launched of RainCube by JPL a smallsat that uses a pulse length of 160 microseconds and chirp to provide superior range resolution and excellent characterization of the transmitted waveform for optimum suppression of the surface return. In our case, we could not rely on such performance of the pulse compression and we employed post-processing that is explained in the manuscript. One last reason why we do not describe the actual system in more detail is because the system is an exact copy of the ground-based version described in Kuechler et al. 2017.

Regarding the scientific content we like to note, that the manuscript is intended for the special issue of the ACLOUD campaign and provides important background for all using these data. Providing some simple macrophysical statistics is thus helpful in putting the measurements into context. Note that the preferred flight altitude of 10000ft in the unpressurized aircraft is due to limitation imposed by the lidar onboard, which is only certified up to this altitude. The issue of liquid water attenuation is important for the planned retrieval development which will also incorporate passive microwave and lidar measurements. Studies addressing this issue will be cited in a revision, e.g., Kuechler et al. 2018 or Meywerk et al. 2005.

On a moving plattform, the unfolding of the Doppler velocity is rather difficult. What would help is a sufficiently good background wind information, that could be used together with the aircraft speed. But unfortunately, no continuous wind profile measurements were available on board Polar 5, and the rather small number of dropsondes doesnt help with that. Using model data has been found to be to inaccurate. Any attempts that have been made so far were not very satisfying. The only cases were we could derive somehow the Doppler velocity is for clouds that have been probed by the aircraft from different directions in rather short time periods.

We agree that over complex terrain the problem of filtering and removing the range lobes is more difficult. Especially the blind zone will be more investigated in future studies. Since we focus only on flights over open ocean, the marginal sea ice zone, and sea ice (all three areas shown in the case study Fig.7), this is not an issue for the measurements taken during the ACLOUD campaign, the recently performed ones during AFLUX, and the upcoming MOSAiC flights. So far, no case has been found in all flights where strong weather echos influenced our method of removing range lobes. We thank the author to point us to this issue and will take special care on this in future campaigns where we might experience stronger weather echos. These arguments will be made more clear in a revised version of the paper.

Reviewer 2

We thank the reviewer very much for her/his detailed thoughts, the very useful comments, and suggestions on the manuscript, and thereby the possibility to further improve it. In the following we will address all major comments and list the changes we made in the manuscript. The section on the chirp tables and the cloud statistics have been remarkably modified to address the reviewers comments. The minor review points will be answered afterwards. In general, the manuscript has been revised and thereby strengthened according to the reviewers comments. Most of the figures have been modified according to the comments and now present the data in an easier readable way. Text that has been revised or that has been added to the manuscript is written in italic letters.

Major or general comments

The first part of Section 2 describes the FMCW radar system itself, the modifications of the ground-based version to the airborne system (basically, reduction of antenna size to fit into the aircraft at the expense of 6dB sensitivity and a wider half power beam width) and gives valuable information regarding issues arising during airborne downward-looking deployment of an FMCW radar and how they can be mitigated (offnadir pointing by 25°) to reduce the ground echo influence. The FMCW radar principle is briefly illustrated and concludes with saying that this study focuses on the analysis of the equivalent radar reflectivity factor although "de-aliasing techniques to unfold Doppler velocity can be applied". - The reader is thus left wondering why this has not been done. (?)

We agree with the reviewer on this point, that the reader is left alone with the statement, because we only mention the possibility to apply de-aliasing techniques to unfold Doppler velocity without applying them and showing any results. As pointed out already in the answer to the first reviewer the unfolding of the Doppler velocity is rather difficult on a moving platform. Attempts to derive a somehow cleaned Doppler velocity gave unsatisfying results and it turned out, that a background wind information is necessary. Ideally, this comes from a continuous measurements like wind lidar. Using wind fields from models has been found to be to inaccurate. The only cases where we could derive somehow the Doppler velocity is for clouds that have been probed by the aircraft from different directions in rather short time periods. Other attempts to unfold the spectrum will be the subject of future studies and campaigns where we try to increase the number of drop sondes for the wind information.

To not leave the reader alone, as the reviewer said, we changed the sentence to: *Although we can apply de-aliasing techniques to unfold the Doppler ve-*

locity, the results have not been satisfying so far. It has been found out, that background wind information is needed to disentangle the Doppler velocity from the aircraft motion. Such information is not available onboard Polar 5. Therefore, we make only use of the equivalent radar reflectivity factor Ze in this study which can be determined from the integral over the Doppler power spectrum..

The capabilities of the FMCW radar allowing for different vertical range resolutions in different chirps are demonstrated for three different chirp programs, however only the characteristics of the first chirp program are discussed. It would be desirable to contrasts the pros and cons of all three used chirp programs.

For the answers to reviewers comments on chirp table see our response to **p.4 lines 33-35**. There we describe the motivation of the three different chirp tables and include some describing text in the manuscript. This should address the question of pros and cons of the chirp tables and why we changed them during the campaign. In addition, the corresponding figure (Fig.1) has been modified so that it is now easier to compare the three chirp tables in terms of maximum range, range gates, and sensitivities.

The description of the passive MWR channels (MiRAC-P) is very technical and even includes a block diagram of the components. Is this done in such a way because it is a first-time deployment of a novel instrument? If so, please state that clearly.

Indeed, it is the first description and deployment of a passive radiometer combining these frequencies in the millimeter and sub-millimeter range. Especially on an aircraft and in the Arctic this has never been done before. In the manuscript this point is now made clear in the beginning of the subsection by: *The passive microwave radiometer MiRAC-P (or RPG-LHUMPRO-243-340) is a unique instrument combining millimeter and submillimeter channels that has been never operated before and especially not the in the Arctic and on an aircraft..*

In Section 3 the different data processing steps are explained in a detailed way. In the radar signal, mirror images are removed and a speckle filter is applied. The description of the filter (p.10 lines 14-26) is sometimes a bit difficult to follow and could benefit from

a re-read and some modifications to improve clarity.

We agree with the reviewer. The paragraph describing the filtering was a bit difficult to read. We re-read the section and made some changes that should make it more easy to read an more understandable. The corresponding paragraph has been changed to: *However, as illustrated in Fig. 5b still some scattered radar reflectivities remain. Thus, processing step II (Table 13) applies a speckle filter which removes isolated signals either remaining from the insufficient mirror image correction that does not take into account higher harmonics or that are due to other processing artifacts. Most important thin isolated horizontal disturbance lines evident in 5b need to be eliminated. The speckle filtering is based on the procedure by Lee et al. (1994a). However, the filter is simplified by considering a radar reflectivity mask, which is defined by setting all radar reflectivities to 1 and everything else to 0. Then, the filter uses a box considering all neighboring measurements around a centered pixel. At a chosen threshold preferably close to 50% of ones the centered value will be set to 0 or will be kept as 1. The aim of the filtering procedure is to remove single speckle pixel and horizontal disturbance lines, which may remain after processing step I. Thus, the box should be as small as possible and should have a rectangular shape tilted by 90° to the horizontal disturbance line comparable to the side-lobes. The value for the time-range is chosen as three because it is the smallest value with a centered time step.Whereas the range-gate-range must be much larger than the time-range, but also an odd number. The observations show that the maximum extent of the disturbance line have an extent of five to six pixels in range-gate direction. Having a filtering-threshold of 50% in mind, the size of the box corresponds to eleven or thirteen range gates, respectively. Taking thirteen range gates for the box gives a better opportunity to fit the threshold to the optimal exclusion of speckle and horizontal disturbance lines. Thus,empirical estimations lead to a threshold of 41.7%. However, a data loss at cloud boundaries is obvious by using such a filter.Figure 5c shows the result of the filtering procedure, which exclude speckle and horizontal disturbance lines.*

The multi-step coordinate transformation to convert from range to altitude is described in a straight-forward way and supported by the appendix. One quick question though: On p.12 line 3 it is mentioned that the sensor location is only known within +-0.5m. This seems like a pretty large uncertainty. What are the reasons for it?

The assumptions on the uncertainties given on p.12 line 3 are rather coarse since we do not know the exact position of the receiver in the radar/belly pod construction in relation to the aircraft center of mass. For the iterative process of finding the true position and alignment we made rather coarse assumptions to be sure it is within the range we search for the true values. In reality it is known with a higher accuracy. Therefore the statement has been changed to: *Within the sensor installation (Sect. 2.3), these parameters are not exactly known and are therefore attributed with some uncertainties.*.

In Section 4 a roughly 30min CloudSat overpass case study over different sea ice conditions is analyzed and the advantages of the lower blind zone and higher spatio temporal resolution of MiRAC is emphasized. The comparison also extends to comparing the brightness temperatures (TB) of the MiRAC-P to the AMSR2-TB-related sea ice concentration product highlighting the ability of MiRAC-P to detect small-scale features like broken sea ice which is not possible by the 6.25 km AMSR2 sea ice product resolution. This comparison is not mentioned in the abstract and should be added there.

We added to the end of the abstract a sentence for the sea ice observation with the MiRAC-A 89 GHz channel. The capabilities of the passive sensor of MiRAC-A for sea ice measurements are part of ongoing studies and will be explored in future campaigns.

In addition, it is possible to get an estimate of the sea ice concentration by the 89 GHz passive channel of MiRAC-A with a much higher resolution than the daily AMSR2 sea ice product on a 6.25 km grid.

Section 5 describes cloud statistics from 19 research flights during ACLOUD. This section can be improved by giving more reasons for surface-type (ice/open ocean) related differences in cloud altitude, observed number of cloud layers, cloud depth, and cloud reflectivities. The CFAD reflectivity plot (Fig 10) has another interesting feature: clouds over ocean exhibit a peak at 0.5-1km at very low reflectivities of below -20dBz. Whats the explanation? Alternatively, Section 5 can be omitted since the paper has a good story line fitting AMT context which can finish after Section 4. Multiple previous ground-based remote-sensing based studies showing frequent occurrence of low-level Arctic clouds - as done in Section 5 -

motivating the need of sensors being able to detect such low clouds already exist. I would suggest the manuscript to be published after minor revision addressing the above-and below points.

We agree with the reviewer that omitting Section 5 and thereby reducing the manuscript to the instrument description and one measurement example would still be enough to be published in and fit the main focus of AMT. Nevertheless, we think that demonstrating the instruments and the setup capabilities by some simple statistical analysis on the observed Arctic clouds and precipitation over different surface types adds some valuable information to the manuscript. But again, as the reviewer says, it needs to be extended and some of the features shown in the figures need to be pointed out in more detail. Therefore, we revised Section 5 completely and included some more extended descriptions and explanations. More focus has been put on the differences between the surface types.

... in Fig. 4 usable for the analysis. Due to the orography of Svalbard and the therefore difficult to interpret measurements, those above land are excluded. Most of the time Polar 5 was flying in an altitude of about 2900 to 3000m, which be seen as well in Fig. 8 where about 80% of all measurements considered in the statistical analysis have been acquired with this flight altitude or above. Figure 8 and Table 11 show as well, that about 57% of the measurements have been taken over open ocean and 43% over sea ice. It has to be kept in mind, that flight patterns have been planed to observe clouds according to numerical weather prediction models. Therefore, the statistics might be biased...

...the cloud fraction vertically resolved in 100m intervals. The highest values are present in the lowest 1000m with about 25 to 30% over sea ice and 30% and above over ocean (solid lines in Fig. 8). The cloud fraction is in general slightly higher over ocean than over sea ice in every height. For measurements at higher levels (above 2850m) the cloud fraction increases which is most likely an artefact since measurements at higher levels where only taken when Polar 5 was forced to climb above clouds due to cloud tops exceeding the typical flight level of 10000ft.

Furthermore a more extensive description of the CFAD figures has been added. These shown interesting features that have been not mentioned so far.

... low amounts of precipitation. A second cluster with lower amount can be found between 500 and 1000m with Z_e values between -20 and -15dBz. Some higher reflectivities around 0dBz can be between 2 and 3km. In contrast measurements over open ocean show higher concentration of reflectivities in the lowest levels between -15 and -8dBz up to 500m and a secondary peak of clouds clustering -25 and -20dBz between 500 and 900m. This second peak not visible over is corresponds to the elevated arctic boundary layer height and the clouds forming here (Chechin and Lüpkes 2019). A band spanning from around -10dBz in 1km to -18dBz at 3km belongs to the vertical extending clouds over ocean. In general ...

Minor comments

p.1 line 15: While it is important to fill the measurement gap of the CloudSat blind zone below 1.5km the phrase "MiRAC is able to fill the gap" seems a bit too strong since MiRAC is an aircraft-mounted instrument and thus limited in time and space and providing several tens of hours of observations during one field experiment instead of continuous coverage. . .please rephrase.

MiRAC measurements can be used to address the question how well CloudSat can sense the lower parts of the atmosphere, i.e., what is the amount of clouds and precipitation missed in low levels in comparison to MiRAC due to the larger blind zone, reduced sensitivity, and lower resolution. Therefore, filling the is more meant to be in terms of understanding and on a case study approach and not in terms of data coverage. We rephrased the sentence so it reads: *...demonstrates that MiRAC with its more than ten times higher vertical resolution down to about 150m above the surface is able to show with some extend what is missed by CloudSat when observing low level clouds..*

p.2 line 3: Osborne et al. - publication year is missing
year of publication has been added

p.2 line 6: Barrow is now called Utqiagvik
first paragraph changed to *...,e.g., Utqiaġvik (formerly known as Barrow), Alaska (Shupe et al., 2015), Ny-Ålesund, Svalbard (Nomokonova et al., 2018), Summit, Greenland (Shupe et al., 2013).*

p.2 line 7: add Summit, Greenland: https://esrl.noaa.gov/psd/arctic/observatories/summit/
has been added (see above)

p.2 line 13: missing citation
added reference for CALIPSO *(CALIPSO; Winker et al., 2003)*

p.2 line 22: Indicate how long the first airborne field experiments in the Arctic date back to
We added: *While a number of airborne campaigns have been performed in the Arctic since the 1980's (Andronache et al., 2017; Wendisch et al., 2018)...*

p.2 line 25: "...Arctic nimbo stratus ice cloud observed during POLARCAT..."
This does not seem necessary since the sentence already mentions POLARCAT.

p.3 line 12: a "Second" without a "first" earlier on
has been changed

p.3 lines 16-19: refer to the photograph of the placement of MiRAC-A and -P on the Polar 5 already here (Fig3)
done

p.4 line 26: You mention the first chirp program is used for the first research flight in Table 1 it is however stated that chirp setting I is used for RF04 and RF05.
sentence changed to: *... used for the first two research flights ...*

p.4 line 29: It sounds contradictory to state that based on the good performance of the chirp program I you modified it twice. . .why modify if performing well?
Indeed the motivation for the different settings was presented too briefly and has been revised the new text is given below together with the next point of the reviewer.

p.4 lines 33-35: Be more precise how you identify the receiver saturation. The sentence b...ackscatter of hydrometeors or the surface echoes are strong enough to shift Z_{min} over the full profile.

is not clear please clarify.
The reviewer is right. We revised the whole paragraph to better explain our motivation for the different chirp settings and the characteristics of the receiver sensitivity. The new text reads as following:

During ACLOUD two different chirp sequences per profile defining the vertical resolution and thus minimum detectable Ze (Z_{min}) were used to account for the fact that the sensitivity of the radar receiver decreases with the distance squared. For the very first flights of MiRAC a conservative vertical resolution was chosen to ensure a high enough sensitivity even if unforeseen problems would arise. With a range resolution of 17.9m over the first 500m (Sequence I in Table 1) Z_{min} decreases from -65dBz at 100m distance from aircraft to about -50dBz in a distance of 600m (Fig. 1). Using a second chirp sequence with a coarser range resolution of 27m for the rest of the profile improves Z_{min} which then again degrades with the distance squared reaching roughly -45dBz at the surface for the typical flight altitude of 3km above ground (Fig. 1). Encouraged by the well-behaved performance of MiRAC with these conservative settings during the first flights the chirp sequences were modified to yield a higher vertical resolution of 4.5m in the first 500m and 13.5m for the rest of the flights (Sequence III in Table 1). Note, that due to higher flight altitudes the chirp settings had to be adapted (Sequence II) in Table 1) to still cover the full column during limited periods.

Figure 1 illustrates exemplary the actually achieved Z_{min} for three research flights with the different chirp settings. Herein, Z_{min} is calculated for each range gate by integrating over the noise power of the Doppler spectrum. Under typical atmospheric conditions this results in the classical behaviour discussed above. However, Figure 1 shows that sometimes deviations can occur which are due to the two following reasons: First, the Doppler spectrum noise power computation fails if the spectral width exceeds the range gates maximum Nyquist velocity. This situation occurs in range gates affected by the strong surface reflectivity and causes the enhanced occurrence of Z_{min} up to -20dBz. Due to different flight altitudes, e.g., clustered around 3.2km for the example in Fig. 1.a, enhanced Z_{min} associated with the surface is spread over different range gates. Second the parallel shifts of Z_{min} profiles are caused by the automatic transmitter power level switching. The radar automatically levels the transmitter power in cases when the input power might lead to receiver saturation effects. The signal power reduction when leads to reduced sensitivity over the whole profile leading to a over the full profile. The automatic power reduction is triggered by high reflections which can occur under certain *flight conditions, e.g., during flight maneuvers leading to a nadir viewing of the radar and thus increased surface backscatter.*

p.8 line 16: add during ACLOUD field experiment
done

p.9 line 18: replace beyond with below
done

p.10 line 3: Second part of the flight is in the marginal sea ice zone...and the first part?
The last two sentences of the paragraph have been changed to *Clearly sub-surface reflection is visible in range gates below the surface especially in the first part of the flight over sea ice (see Fig. 7 for sea ice cover) with similar characteristics in the corresponding range gates above the surface. The second part of the flight leg is less affected which can be attributed to a change in surface characteristics of the marginal sea ice zone and open water.* with including a reference to the figure showing the sea ice coverage of the flight section.

p.11 line 11: at the expense
changed

p.15 line 13: add AMSR2 before sea ice product
done

p.15 line 29: 25m vertical resolution only refer to chirp program I in Table 1, correct?
It is true, this is only valid for chirp III. The sentence has been reformulated to: *...reaches a vertical extent greater than 25m, which roughly correspond to two range gates for chirp table III (or one range gate for chirp I and II, Table 11).*

p.17: the sea ice concentration of Bremen? There is sea ice in Bremen? ;) Please correct.
That was misleading. Changed to *AMSR2* sea ice concentration.

p.17 line 10: The sentence regarding the number of measurements above sea ice is increased with respect to number of measurements

above open ocean is unclear. Do you mean is higher?
Sentence changed to: *The number of measurements above sea ice and broken sea ice is higher than the number of measurements over open ocean (Fig.8).*

p.17 line 12: Deriving a cloud depth over sea ice lower than 800m from Fig.9 seems a bit arbitrary...
After reconsidering the statement we decided to remove it.

Figures

Please check Figure quality (Fig6+7 have low resolution) and make sure all figures have proper axis labels with a variable and units (Fig.1, Fig.4, Fig.5).
done

Fig.1: Why is there an extra colorbar in the middle panel?
It is not an extra colorbar. This colorbar gives the frequency of sensitivities. Unfortunately, most of the values are close to 0. Therefore, it looks like there is no connection between colorbar and data. We redesigned the figure. Now it is more clear.

Fig.7: Add the Channel frequencies in the lower three panels to increase comparability between figure and description in the text.
done with adapted caption. The channels numbers have been removed as well in Table 16, since they are obsolete now.

References

- N. Kchler, S. Kneifel, P. Kollias, and U. Lhnert. Revisiting Liquid Water Content Retrievals in Warm Stratified Clouds: The Modified Frisch. Geophysical Research Letters, 45(17):9323 9330, 2018.
- N. Kchler, S. Kneifel, U. Lhnert, P. Kollias, H. Czekala, and T. Rose. A W-band radarradiometer system for accurate and continuous monitoring of clouds and precipitation. Journal of Atmospheric and Oceanic

Technology, 34(11):23752392, 2017.

- J. Meywerk, M. Quante, and O. Sievers. Radar based remote sensing of cloud liquid water application of various techniques a case study. Atmospheric Research, 75(3):167181, 2005

Microwave Radar/radiometer for Arctic Clouds MiRAC: First insights from the ACLOUD campaign

Mario Mech[1], Leif-Leonard Kliesch[1], Andreas Anhäuser[1], Thomas Rose[2], Pavlos Kollias[1,3], and Susanne Crewell[1]

[1]Institute for Geophysics and Meteorology, University of Cologne, Cologne, Germany
[2]Radiometer-Physics GmbH, Meckenheim, Germany
[3]School of Marine and Atmospheric Sciences, Stony Brook University, NY, USA

Correspondence: Dr. Mario Mech, Institute for Geophysics and Meteorology, University of Cologne, Pohligstr. 3, 50969 Cologne, Germany (mario.mech@uni-koeln.de)

Abstract. The Microwave Radar/radiometer for Arctic Clouds (MiRAC) is a novel instrument package developed to study the vertical structure and characteristics of clouds and precipitation onboard the Polar 5 research aircraft. MiRAC combines a frequency modulated continuous wave (FMCW) radar at 94 GHz including a 89 GHz passive channel (MiRAC-A) and an eight channel radiometer with frequencies between 175 and 340 GHz (MiRAC-P). The radar can be flexibly operated using different chirp sequences to provide measurements of the equivalent radar reflectivity with different vertical resolution down to 5 m. MiRAC is mounted for down-looking geometry on Polar 5 to enable the synergy with lidar and radiation measurements. To mitigate the influence of the strong surface backscatter the radar is mounted with an inclination of about 25° backward in a belly pod under the Polar 5 aircraft. Procedures for filtering ground return and range side-lobes have been developed. MiRAC-P frequencies are especially adopted for low humidity conditions typical for the Arctic to provide information on water vapor and hydrometeor content. MiRAC has been operated on 19 research flights during the ACLOUD campaign in the vicinity of Svalbard in May/June 2017 providing in total 48 hours of measurements from flight altitudes > 2300 m. The radar measurements have been carefully quality controlled and corrected for surface clutter, mounting of the instrument, and aircraft orientation to provide measurements on a unified, geo-referenced vertical grid allowing the combination with the other nadir pointing instruments. An intercomparison with CloudSat shows good agreement in terms of cloud top height of 1.5 km and radar reflectivity up to -5 dBz and demonstrates that MiRAC ~~is able to fill the gap in observing low level clouds~~ with its more than ten times higher vertical resolution down to about 150 m above the surface is able to show to some extend what is missed by CloudSat when observing low level clouds. This is especially important for the Arctic as about 40 % of the clouds during ACLOUD showed cloud tops below 1000 m, i.e., the blind zone of CloudSat. In addition, with the MiRAC-A 89 GHz it is possible to get an estimate of the sea ice concentration with a much higher resolution than the daily AMSR2 sea ice product on a 6.25 km grid.

1 Introduction

In the rapidly changing Arctic climate (e.g., Serreze et al., 2009; Graversen et al., 2008), the role of clouds and associated feedback remain unclear (?Wendisch et al., 2017)(Osborne et al., 2018; Wendisch et al., 2017). In particular, understanding the effect of mixed-phase clouds whose persistence is controlled by a complex interaction of microphysical, radiative, and dynamic processes is still challenging (Morrison et al., 2012). Information on their vertical structure and phase partitioning which control their radiative impact (Curry et al., 2002) is currently available from the few ground-based profiling sites in the Arctic, e.g., Barrow, Alaska (Shupe et al., 2015)Utqiaġvik (formerly known as Barrow), Alaska (Shupe et al., 2015), Ny-Ålesund, Svalbard (Nomokonova et al., 2018) , Summit, Greenland (Shupe et al., 2013). The use of synergistic lidar and cloud radar measurements are key for the study of these cloud systems. Passive microwave measurements further provide information on the vertically integrated liquid water path (LWP). The profiling sites provide important long-term statistics, however, they might be limited in their representativity for the wider Arctic.

Polar-orbiting, passive satellite imagery provides coverage of the Arctic region, however, the retrieval of cloud properties is challenged by the surface properties and suffer from limited vertical information. Active space-borne measurements by lidar and radar, i.e., by the combination of Cloud-Aerosol Lidar and Infrared Pathfinder Satellite Observation (Winker et al., 2003, CALIPSO;) and CloudSat (Stephens et al., 2009) have been fundamental in better understanding the vertical structure of clouds around the globe. However, the CloudSat Cloud Profiling Radar (CPR) provides limited information in the lowest 0.75 to 1.25 km due to the presence of strong surface echo (Maahn et al., 2014; Burns et al., 2016), while the CALIPSO lidar observations are often fully attenuated by the presence of supercooled liquid layers. Using CALIPSO and CloudSat measurements Mioche et al. (2015) identified the region around Svalbard to be particularly interesting to study mixed-phase clouds as these show here a higher frequency of occurrence (55 %) compared to the Arctic average (30%30 % in winter and early spring, 50 % May to October).

Airborne platforms have the advantage of high spatial flexibility and accessibility of remote places comparable to satellite observations. While a number of airborne campaigns have been performed in the Arctic (Andronache, 2017; Wendisch et al., 2018) the use of radar/lidar system in these aircraft campaigns is rather limited. One notable exception was during the Polar Study using Aircraft, Remote Sensing, Surface Measurements and Models, of Climate, Chemistry, Aerosols, and Transport (POLARCAT) campaign in spring 2008, Delanoë et al. (2013) studied an Arctic nimbo stratus ice cloud using the French airborne radar–lidar instrument in detail.

During May/June 2017 the Arctic CLoud Observations Using airborne measurements during polar Day (ACLOUD; Wendisch et al., 2018; Knudsen et al., 2018) aircraft campaign was performed as part of the ArctiC Amplification: Climate Relevant Atmospheric and SurfaCe Processes, and Feedback Mechanisms project ($(AC)^3$; Wendisch et al., 2017). The research aircraft Polar 5 and 6 of the Alfred Wegener Institute (AWI) operating from Longyearbyen, Svalbard, deployed a remote sensing and in-situ microphysics instrument package, respectively. Polar 5 was equipped with the Airborne Mobile Aerosol Lidar for Arctic research (AMALi; Stachlewska et al., 2010) and spectral solar radiation measurement already operated during the VERtical Distribution of Ice in Arctic clouds (VERDI; Schäfer et al., 2015) campaign. During ACLOUD, the remote sensing package was complemented by the novel Microwave Radar/radiometer for Arctic Clouds (MiRAC). In contrast to most other millimeter radars employed on research aircraft (e.g., Radar Aéroporté et Sol de Télédétection des propriétés nuAgeuses (RASTA; Delanoë et al., 2012), High-performance Instrumented Airborne Platform for Environmental Research (HIAPER) Cloud Radar (HCR; Rauber et al., 2017), Wyoming Cloud Radar (WCR; Khanal and Wang, 2015), High Altitude and LOng range research aircraft Microwave Package (HAMP; Mech et al., 2014)), which use short microwave pulses for ranging, the radar of the MiRAC package employs a Frequency Modulated Continuous Wave (FMCW) radar. Thus a lower peak power transmitter is used, however, carefully consideration on handling the surface return is required. Therefore, in the past airborne FMCW radar has been mounted in uplooking geometry (Fang et al., 2017).

The purpose of this study is two-fold. First, the MiRAC package which consists of a unique 94 GHz FMCW radar (MiRAC-A) and an eight channel passive microwave radiometer with channels between 170 and 340 GHz (MiRAC-P) is introduced. The instrument specifications and integration into the Polar 5 aircraft in downward looking geometry are provided in Sect. 2 ~~. The~~ followed by the methodology used to quality control and mapping the observations to a geo-referenced coordinate system ~~is described~~ in Sect. 3. ~~Second, the~~ The performance of the MiRAC during its first deployment within ACLOUD will be demonstrated ~~first~~ via a comparison with CloudSat within a case study in Sect. 4 and a short statistical analysis of the ACLOUD measurements is shown in Sect. 5. Conclusions and outlook to further analysis and deployments of MiRAC ~~is~~ are given in Sect. 6.

2 Instruments and aircraft installation

MiRAC is composed of an active (~~MIRAC-A~~MiRAC-A) and passive (MiRAC-P) part. MiRAC-A is mounted between the wings of the research aircraft Polar 5 and MiRAC-P is mounted inside of the aircraft measuring through a sufficient large aperture (see Fig. 3). Since, the FMCW radar needs a different measuring angle, MiRAC-A is tilted by ~~25 °~~ 25° backwards with respect to nadir, whereas MiRAC-P is nadir-looking. The following three sections will describe the instruments and aircraft installation in detail.

2.1 FMCW W-band radar

MiRAC-A is based on the novel single vertically polarized cloud radar RPG-FMCW-94-SP manufactured by RPG-Radiometer Physics GmbH which is described in detail by Küchler et al. (2017). It basically consists of a transmitter with adjustable power to protect the receiver from saturation, a Cassegrain two-antenna system for continuous signal transmission and reception, and a receiver containing both the radar receiver channel at 94 GHz and the passive broadband channel at 89 GHz. To guarantee accurate measurements both channels are thermally stabilized within a few mK. The FMCW principle allows to achieve high sensitivity for short range resolutions down to 5 m with low transmitter power of about 1.5 W from solid state amplifiers. The radar is also equipped with a passive channel at 89 GHz using the same antenna as the radar. The radar has been calibrated to provide the equivalent radar reflectivity Z_e with an uncertainty of 0.5 dBz. The uncertainty of the brightness temperature (TB) measured by the 89 GHz channel is ±0.5 K (Küchler et al., 2017).

The cloud radar has originally been developed for ground-based application. Here the passive channel is especially useful because liquid water strongly emits at 89 GHz and with the cosmic background temperature as a low and well known background signal the LWP can be derived from TB measurements. As explained in the next subsection the strong and highly variable emissivity of the surface complicates LWP retrieval from the airborne perspective. However, it additionally provides information about the presence of sea ice exploited from satellite (Spreen et al., 2008).

For the installation on the Polar 5 aircraft, the radar's antenna aperture size had to be reduced from 500 mm down to 250 mm in order to accommodate the radar into the Polar 5 belly pod. This implies a sensitivity loss of 6 dB compared to the original RPG-FMCW-94-SP design. The smaller antenna size implies a wider half power beam width (HPBW) of 0.85° (antenna gain approx. 47 dB). The quasi bi-static system's 90 % beam overlap (beam separation of 298 mm) is achieved in a distance of 75 m from the radar (compared to 280 m for the 500 mm aperture radar). Therefore, measured Z_e profiles start in 100 m distance from the aircraft.

In the case of aircraft deployments, the radar's receiver can be easily run into saturation caused by strong ground reflections when pointing nadir, due to the fact that a FMCW radar continuously emits and receives signal power. A pulsed radar overcomes this problem, because the strong ground reflection pulse does not affect the atmospheric reflection signals, which are received delayed in time relative to the ground pulse. Therefore, the antenna axis of a down looking FMCW radar deployed on an aircraft must be tilted against the nadir axis, so that the ground reflection becomes significantly attenuated. A comprehensive analysis of sufficient inclination viewing angles relative to nadir for FMCW radar observations is given in Li (2005). The Polar 5 radar has been tilted by 25° from nadir backwards, following the guidelines in Li et al. (2005).

For an FMCW radar, ranging is achieved by transmitting saw tooth chirps with continuously increasing transmission frequency over a given sampling time and frequency bandwidth. The time difference between transmission and reception of a given frequency provides the range resolution. If the radar signal is backscattered by a particle moving towards or away from the radar an additional frequency shift much smaller than one from ranging occurs due to the Doppler effect. The Doppler spectrum for each range gate yields from the radar processing involving two Fast Fourier Transformations (FFT). For an airborne radar the Doppler spectrum is difficult to interpret due to the Doppler effect induced by aircraft motion (Mech et al., 2014). Although we can apply de-aliasing techniques to unfold the Doppler velocity, here the results have not been satisfying so far. It has been found out, that background wind information is needed to disentangle the Doppler velocity from the aircraft motion. Such information is not available onboard Polar 5. Therefore, we make only use of the equivalent radar reflectivity factor Z_e in this study which can be determined from the integral over the Doppler power spectrum.

During ACLOUD two different chirp sequences per profile defining the vertical resolution and thus minimum detectable Z_e (Z_{min}) were used to account for the fact that the sensitivity of the radar receiver decreases with the distance squared. For the very first flights of MiRAC a conservative vertical resolution was chosen to ensure a high enough sensitivity even if unforeseen problems would arise. With a range resolution of 17.9 m over the first 500 m as used for the first research flight ((Sequence I in Table 11) Z_{min} decreases from -65 dBz at 100 m distance from aircraft to about -50 dBz in a distance of 600 m (Fig. 1). Using a second chirp sequence with a coarser range resolution of 27 m for the rest of the profile improves Z_{min} which then again degrades with the distance squared reaching roughly -45 dBz at the surface for the typical flight altitude of 3 km above ground (Fig. 1). Based on the good performance achieved for these settings 1). Encouraged by the well-behaved performance of MiRAC with these conservative settings during the first flights the chirp sequences were modified twice during ACLOUD to achieve even finer range resolution (to yield a higher vertical resolution of 4.5 m in the first 500 m and 13.5 m for the rest of the flights (Sequence III in Table 11). Note, that due to higher flight altitudes the chirp settings had to be adapted (Sequence II in Table 11) to still cover the full column during limited periods.

Figure 1 illustrates exemplary the actually achieved Z_{min} for three research flights with the different chirp settings. Herein, Z_{min} is calculated for each profile using individual power measurements. In addition to range gate by integrating over the noise power of the Doppler spectrum. Under typical atmospheric conditions this results in the classical behaviour discussed abovetwo features emerge. . However, Fig. 1 shows that sometimes deviations can occur which are due to the two following reasons: First, the strong surface backscatter yields saturation effect in the receiverDoppler spectrum noise power computation fails if the spectral width exceeds the range gate's maximum Nyquist velocity. This situation occurs in range gates affected by the strong surface reflectivity and causes the enhanced occurrence of Z_{min} up to -20 dBz. Due to different flight altitudesthe decrease , e.g., clustered around 3.2 km for the example in Fig. 1 I, enhanced Z_{min} associated with the surface is spread over different range gates. Second , in some cases backscatter of hydrometeors or the surface echoes are strong enough to shift Z_{min} over the full profile. the parallel shifts of Z_{min} profiles are caused by the automatic transmitter power level switching. The radar automatically levels the transmitter power in cases when the input power might lead to receiver saturation effects. The signal power reduction then leads to reduced sensitivity over the whole profile. The automatic power reduction is triggered by high reflections which can occur under certain flight conditions, e.g., during flight maneuvers leading to a nadir viewing of the radar and thus increased surface backscatter.

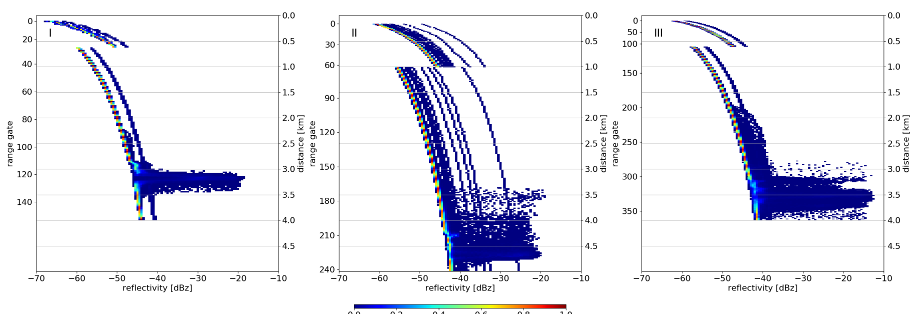

Figure 1. Sensitivity limit in [dBz] (Z_{min}) for vertical polarization of different chirp tables with different vertical resolution as a function of distance from the aircraft (secondary y-axes) for the three settings used during ACLOUD. The vertical resolution increases from a) left to cright (I to III) with increasing number of range gates, a: (I) 154 range gates, May 25, 08:58 - 12:19 UTC, RF05, b(II) 242 range gates June 23, 12:53 - 13:43 UTC, RF22, c(III) 364 range gate May 27, 08:14 - 11:04 UTC, RF06.

2.2 Passive millimeter and sub-millimeter radiometer

The passive microwave radiometer MiRAC-P (or RPG-LHUMPRO-243-340) is a unique instrument combining millimeter and submillimeter channels that has been never operated before and especially not in the Arctic and on an aircraft. In contrast to the MiRAC radar, the passive microwave channels deployed on the Polar 5 aircraft ~~(RPG-LHUMPRO-243-340)~~ are pointing nadir with respect to the aircraft fuselage. In order to co-align radar and passive observations, the atmospheric signal delay caused by the radar tilt must be taken into account by correcting for the aircraft's horizontal speed. For reference, a detail description of MiRAC-P is provided below.

MiRAC-P consists of a double sideband (DSB) receiver with six channels centered around the 183.31 GHz water vapor (WV) line and two window channel receivers at 243 and 340 GHz. The schematic in Fig. 2 shows the overall system layout. The received radiation enters the radiometer through a low loss radome window (attenuation at 180 GHz approx. 0.01 dB) and is then reflected by an off-axis parabola antenna onto a wire grid beam splitter, forming beams between 1.3 ~~°~~ and 1° (Table 12). The vertical polarization is transmitted into the 183.31 GHz water vapor receiver (WVR) while the horizontal polarization is further split in frequency by a dichroic plate, separating the 243 from the 340 GHz channel. All receivers are of DSB heterodyne type utilizing sub-harmonic mixers as the frontal element. The local oscillators (LOs) consist of Phase Locked Loop PLL stabilized fundamental dielectric resonant oscillators (DROs), multiplied by several active frequency multiplier stages as shown in Fig. 2. The frequency stability of these oscillators is close to 10^{-7} K^{-1}.

The WVR is equipped with a secondary standard, a noise switching system periodically injecting a precise amount of white noise power to the receiver input. By assuming a stable constant noise power over time, receiver gain fluctuations are effectively cancelled (noise adding radiometer, see Ulaby et al. (1981)). Unfortunately, state of the art noise sources with reasonable power output of at least 13 dB excess noise ratio are currently limited to maximum frequencies around 200 GHz, so that the two window channels (243 and 340 GHz) cannot use and benefit from them.

The WVR's Intermediate Frequency (IF) architecture is a six channel filter-bank design with the characteristics given in Table 12. All channels are acquired simultaneously (100 % duty cycle) by using a separate detector for each channel with 1 s temporal resolution. The window channel's IF bandwidth (BW) is 1950 MHz for both 243 and 340 GHz. Because of the DSB mixer response, this corresponds to twice as much signal bandwidth of about 4 GHz (Table 12) having a small gap of 100 MHz in the center. Both sidebands are combined in the mixer IF output signal, so that a flat mixer sideband response is essential, meaning the mixer sensitivity and conversion loss must be almost identical in both sidebands. The subharmonic mixer design is optimal in this respect offering a sideband conversion loss balance of better than 0.1 dB. The most demanding receiver in terms of sideband balance is the WVR due to its overall signal bandwidth of 15 GHz. The benefit of the DSB receiver design is a more than doubled radiometric sensitivity compared to a SSB (Single Sideband) receiver.

The parabolic mirror at the optical input can be turned to all directions for scanning purposes (sky view) or to point to the internal ambient temperature precision calibration target (accuracy 0.2 K). The WVR uses this target to determine drifts in receiver noise temperature while the 243 / 340 GHz channels are correcting for gain drifts. Typically, calibration cycles are repeated automatically every 10 to 20 min by the radiometer's internal control PC. These long intervals are possible because of a dual stage thermal control system, stabilizing the receiver's physical temperatures to better than 30 mK over the whole environmental temperature range (-30 to +45°C). Given the receiver noise temperatures T_R (Table 12) and the integration time of 1 s measurement noise is below 0.5 K.

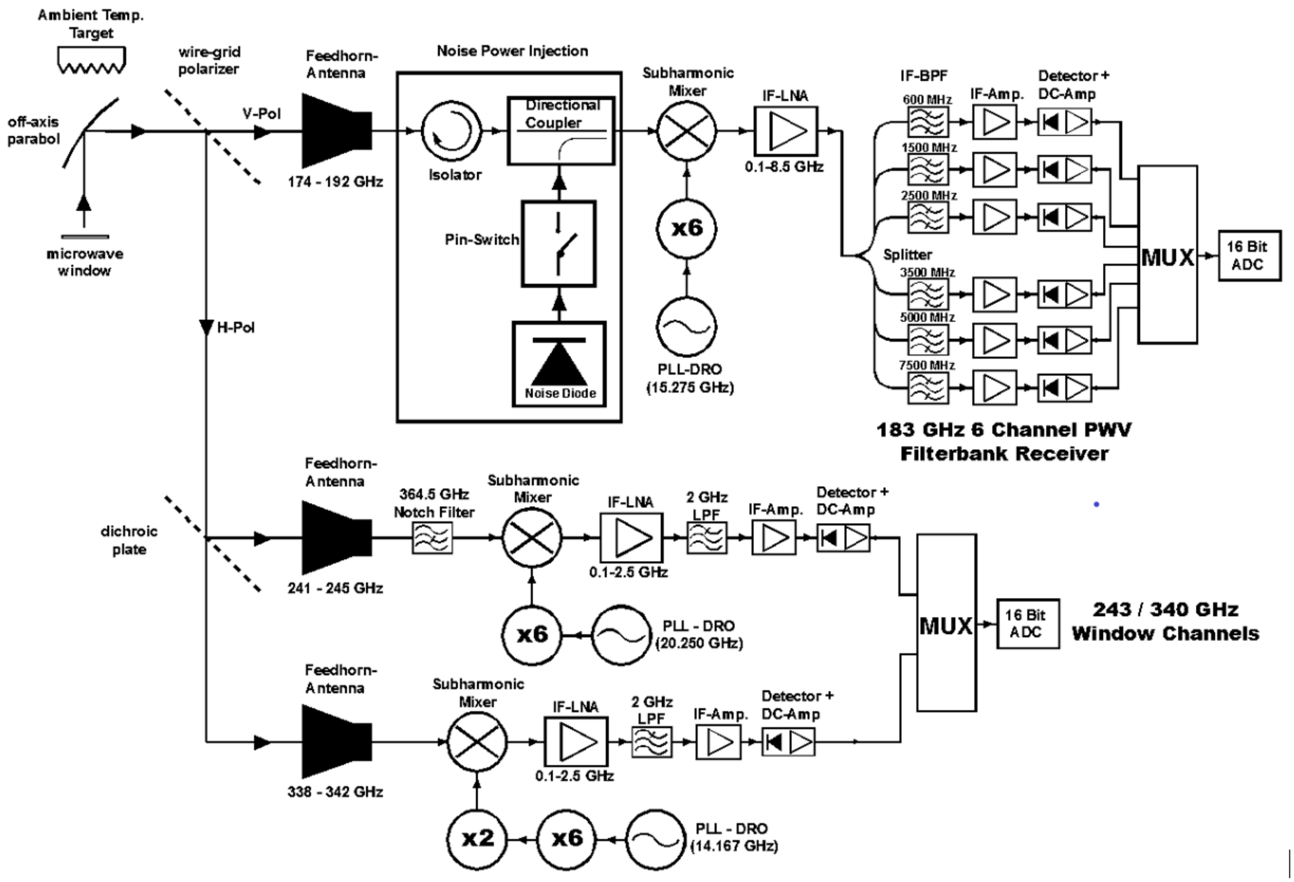

Figure 2. Block diagram of MiRAC-P.

2.3 Installation and Aircraft Operation

The Polar 5 aircraft is a Basler BT-67 operated by the Alfred Wegener Institute for Polar and Oceanic Research (Wesche et al., 2016). In addition to MiRAC, the AMALi lidar and radiation sensors were integrated into the Polar 5. To provide accurate information on the aircraft position an inertial navigation system is used which provides as well information on aircraft orientation, i.e., pitch ϵ, roll ρ, and heading η angles.

Due to the simpler electronic design and lack of high-voltage components compared to pulsed systems the FMCW radar has relatively small dimensions of 83cm $\times$ 57cm $\times$ 42cm and weight of 88 kg allowing a relatively simple integration into the Polar 5 aircraft. As cabin space and openings are limited a special belly pod has been designed to accommodate MiRAC-A

(Fig. 3) below the aircraft. The belly pod with a size of 200cm × 89cm × 50cm has been designed and fabricated by Lake Central Air Services. Openings of 27 cm in diameter for transmitter and receiver antenna allows an unstopped view of MiRAC exposing the radomes directly to the environment. When grounded the aircraft fuselage is tilted by roughly 14° and the radar is integrated in the belly pod such that the pointing is about 25° backward during typical flight operation. The exact mounting position of the radar with respect to the aircraft is derived by a calibration method, which requires a calibration flight pattern, in which roll and pitch angle as well as flight altitude are changed rapidly over calm ocean. Further insight of determining the mounting position are described in Sect. 3.2.

In contrast to the radar MiRAC-A, MiRAC-P is integrated to Polar 5 roughly pointing at nadir during flight. While in ground based operation MiRAC-P can be mounted on a stand with the microwave transparent radome oriented towards zenith (Rose et al., 2005) here the radiometer box is fixed head over directly to the floor of the aircraft cabin (Fig. 3) looking through an opening in the fuselage. In this way the radome is directly exposed to the air avoiding any attenuation. In order to co-align radar and passive observations, the atmospheric signal delay caused by the radar tilt must be taken into account by correcting for the aircraft's horizontal speed. To protect the instruments during start and landing the instrument compartment including MiRAC-P underneath the Polar 5 is protected via flexible roller doors.

For both passive components, MiRAC-P and the receiver at 89 GHz of MiRAC-A, absolute calibrations with liquid nitrogen have to be performed before the first flight after the installation as described in Rose et al. (2005) and Küchler et al. (2017). This procedure has to be repeated whenever the instruments are without power for longer period or are flown in significantly different conditions. On ground the instruments are constantly heated to keep conditions stable for the receiver parts.

MiRAC has been operated successfully on 19 research flights (RF) during the ACLOUD field experiment with significant data loss occurring only during RF13 on June 5 2017 due to software problems. Though some flights were flown close to the ground for albedo and flux measurements, more than 50 % of the flight time was dedicated to straight legs above 2300 m altitude (pitch angle $\epsilon < 10°$ and roll $|\rho| < 3°$) allowing to probe a large range of different cloud conditions, e.g., over ocean, the marginal sea ice zone, and closed ice (Fig. 4). A special focus has been put on flights in the vicinity of the research vessel Polarstern that has set up an ice-floe camp North-West of Svalbard in the framework of the Physical feedback of Arctic boundary layer, Sea ice, Cloud and AerosoL (PASCAL) campaign (Wendisch et al., 2018) between June 5 and 14 2017.

3 Data processing

~~All variables measured by MiRAC are recorded in the sensor-relative coordinate system. For scientific analysis, however, data with geographic coordinates longitude λ , latitude ϕ and altitude h are needed~~In total five processing steps convert the raw data to the final geo-referenced data product (Table 13). First, a methodology to identify and remove range side-lobe artifacts ~~introduced~~ induced by the strong surface echo return is developed (Sect. 3.1) and applied to the MiRAC-A observations on its native coordinate system. Second,provide an explicit ~~analytical~~ analytically method to map data from aircraft-relative to ~~local~~ Earth-relative coordinates~~which we extended~~. Here, we extended their method to fit our purpose (Sect. 3.2). ~~In total five processing steps convert the raw data to the final geo-referenced data product (Table 13). Their effect for a radar time series~~

Figure 3. Left: MiRAC-A with opened belly pod below the research aircraft Polar 5. Right: MiRAC-P eight channel radiometer mounted in the aircraft cabin.

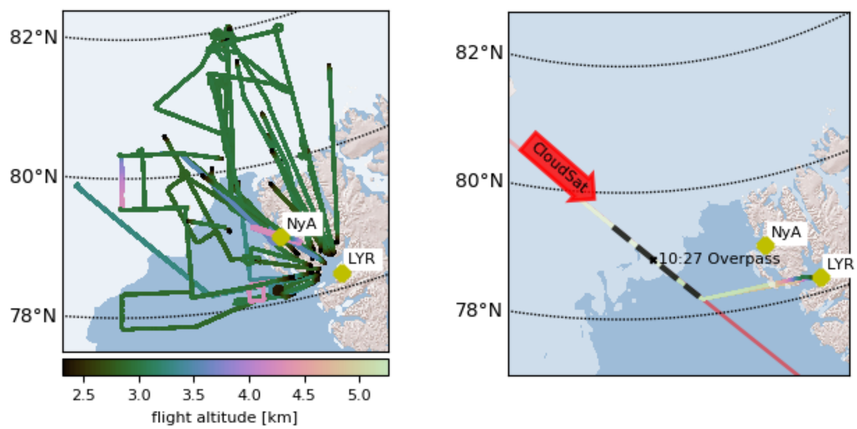

Figure 4. Left: tracks of all research flights of Polar 5 during ACLOUD around Svalbard with an altitude h (above sea level) larger than 2.3 km, $\epsilon < 10°$, and $|\rho| < 3°$. Right: Polar 5 CloudSat underflight on May 27 between 10:06 and 10:44 UTC West of Svalbard. In red the CloudSat track is shown.The white colored area shows the 15 % sea ice coverage derived from AMSR2 observations.

~~is illustrated for a case study (~~All variables measured by MiRAC are recorded in the sensor-relative coordinate system. For scientific analysis, however, data with geographic coordinates longitude λ , latitude ϕ and altitude h are needed. All processing steps are illustrated in Fig. 5 ~~)~~for an exemplary radar reflectivity time series.

3.1 Filtering of range side-lobes artifacts

The filtering described here identifies and removes non-meteorological artifacts in the radar reflectivity observations induced by range side-lobes. The slant distance of the aircraft to the surface can easily be identified from the range gate with the strongest Z_e, which is associated with the surface return. The strength of the surface radar return depends on the type of surface (~~land, sea-ice or sea~~ i.e. land, sea ice, broken sea ice, or open water) and wind speed. The FFT of piece-wise continuously differentiable functions lead to overshooting waves at discontinuities. This phenomenon is called Gibb's phenomenon. ~~In context to~~ The Gibb's phenomenon explains the range side-lobes appearing near by the strong surface radar reflectivity signal~~, range side-lobes can occur in range gates further away and lead to a contamination of the cloud profile~~. The effect depends on the filter characteristics of the FFT used in signal processing which typically produce symmetric side-lobes. While range gates above the surface can include contributions from both the atmosphere and the surface, the "mirror signal" ~~beyond~~ below the surface is only produced by the leakage of the surface return. This is illustrated for an one hour time series in Fig. 5a. Clearly ~~sub-surface reflection~~ a side-lobe is visible in range gates ~~beyond~~ below the surface especially in the first part of the flight over sea ice (see Fig. 7 for sea ice cover) with similar characteristics in the corresponding range gates above the surface. ~~Note, that the~~ Hence, there are two horizontal disturbance lines in time, which are "mirrored" at the surface signal. The second part of the flight leg is less affected which can be attributed to a change in surface characteristics ~~in~~ of the marginal sea ice zone and open water.

The ~~first~~ processing step I (Table 13) includes the removal of the mirror image, which is also called sub-surface reflection filter ~~. Herein~~ in Table 16 of the appendix. Herein, the below surface range ~~side-lobes are~~ side-lobe is quantified and subsequently subtracted from both range side-lobes. For this subtraction of the mirror signal we assume that both range side-lobes above and below the surface are ~~nearly similar~~ equal which is justified by the symmetry of the digital FFT filter function. The subtraction method is defined by considering the environment of every single time-step. At each time step ~~also the~~ three measurements before and after are considered to locate the sub-surface reflection, the mirrored signal below the surface, and its vertical extent. Within the located sub-surface reflection the value of the highest disturbance is used as subtracted value. The extent ~~and~~ of the sub-surface reflection and its distance from the highest reflectivity signal of the surface to the center of the sub-surface reflection provides the ~~extent and~~ distance to locate the range ~~side-lobes~~ side-lobe and its extent above the surface.

However, as illustrated in Fig. 5b still some scattered radar reflectivities remain. Thus, processing step II (Table 13) applies a speckle filter which removes isolated signals either remaining from the insufficient mirror image correction that does not take into account higher harmonics or that are due to other processing artifacts. Most important thin isolated ~~lines evident~~ horizontal disturbance lines evident in 5b need to be eliminated.

The speckle filtering is based on the procedure by Lee et al. (1994a). However, the filter is simplified by considering a radar reflectivity mask, which is defined by setting all radar reflectivities to 1 and everything else to 0. Then, ~~a box is defined to consider~~ the filter uses a box considering all neighboring measurements around a centered pixel. At a chosen threshold preferably close to 50 % of ones the centered value will be set to 0 or will be kept as 1. The aim of the filtering procedure is to remove single speckle pixel and horizontal disturbance lines, which may remain after processing step I. Thus, the box should be as small as possible and should have a rectangular shape tilted by 90° to the horizontal disturbance line comparable to the side-lobes. The value for the time-range is chosen as three because it is the smallest value with a centered time step. Whereas the range-gate-range must be much larger than the time-range, but also an odd number. The observations show that the maximum extent of the disturbance line have an extent of five to six pixels in range-gate direction. ~~This corresponds to a box with~~ Having a filtering-threshold of 50 % in mind, the size of the box corresponds to eleven or thirteen range gates, respectively~~, if the threshold for neighbors is close to~~. Taking thirteen range gates for the box gives a better opportunity to fit the threshold to the optimal exclusion of speckle and horizontal disturbance lines. Thus, empirical estimations lead to a threshold of 41.7 %. However, a slight data loss at cloud boundaries ~~always occurs~~ is obvious by using such a filter. Figure 5c shows the result of the filtering procedure, which exclude speckle and horizontal disturbance lines.

Close to the surface the contamination by the surface reflection is too high to apply a correction. Therefore the lowest 150 m to the surface need to be ignored (Fig. 5f, grey shading). Further information of the filtered values can be found in the appendix (Table 16).

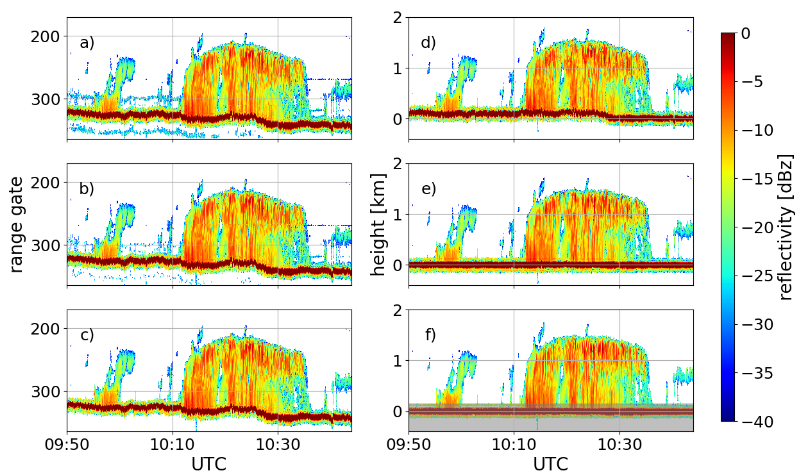

Figure 5. Time series of Z_e profiles measured during RF06 on May 27 2017 for different processing steps (see Table 13): a) raw data, b) after subtraction of mirror signal, c) after speckle filter, d) filtered data on a time-height grid, e) corrected for sensor altitude, mounting position, pitch and roll angle, f) remapping onto a constant vertical grid. The grey shading indicates the range of surface contamination ($\leq$ 150 m).

3.2 Coordinate transformation

For the conversion of the measurements into the geographical coordinate system the approach by Lee et al. (1994b) is extended and generalized. Two additional frames of reference are introduced. First, the sensor related coordinate system, in which the data are recorded and which is not identical to the platform (= airframe) coordinates. Second, the global geographic coordinate (λ, ϕ, h) system, which is used in many applications and is of equal interest as the local Earth-relative coordinate (local East, North, zenith) system.

Then, the technique by establishing a mathematical object called *transform* that performs coordinate transformations between different reference frames is generalized. It can be inverted and composed, providing a simple formalism for multi-step coordinate transformations. Furthermore, it can be easily implemented in object oriented programming languages. The generalization comes ~~to~~ at the expense of a slightly elevated level of abstractness. A detailed description is provided in the appendix.

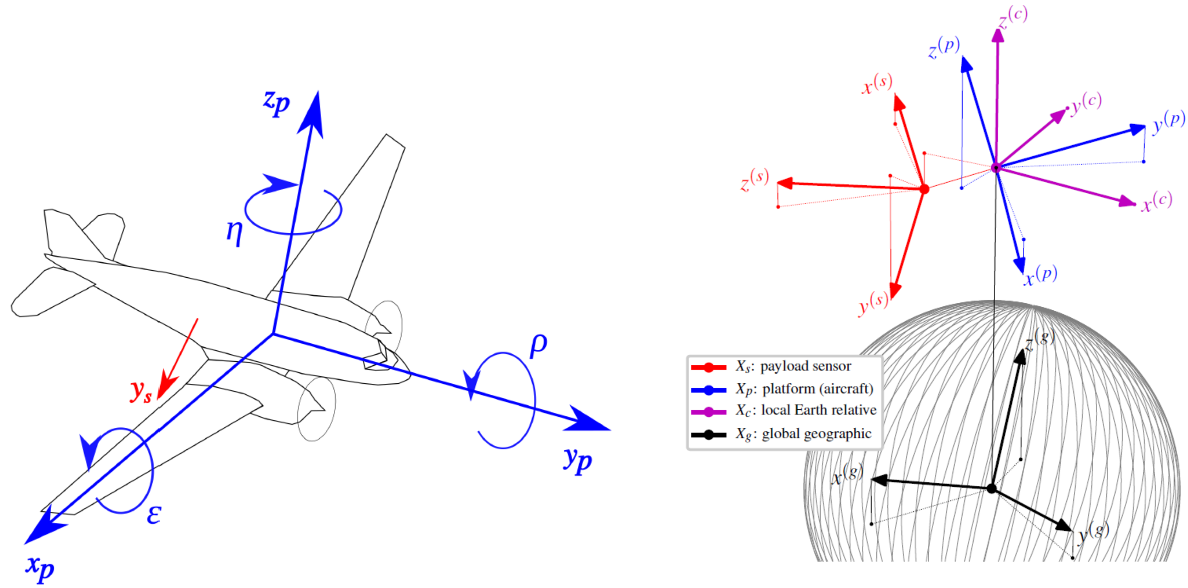

Figure 6. Left: sketch of the Polar 5 aircraft and the platform-relative X_p reference frame. Right: reference frames for airborne measurements: sensor-relative X_s (red), platform-relative X_p (blue), local Earth-relative X_c (purple), and global geographic (black). The grey lines are meridians of X_g and the sphere they indicate may be seen as the planet surface, but distances are obviously not to scale. *Blue:* Coordinate axes of the aircraft reference frame X_p and principal rotation angles: heading η, pitch ϵ, and roll ρ. *Red:* y-axis of X_s.

The coordinate transformation from the payload sensor-relative reference frame X_s to the global geographic reference frame X_g, i.e., processing step III (Table 13), is done via two intermediate reference frames. First, the coordinates are transformed from X_s to the platform-relative reference frame X_p. Then a transformation to the local Earth-relative reference frame X_c is performed. Finally, the coordinates are transformed from X_c to X_g. The origins and orientations of the reference frames are defined in Table 14 and visualized in Fig. 6. If possible, the definitions of Lee et al. (1994b) are adopted.

The mathematical basis of the coordinate transformation and its application is described in detail in the appendix (A). Basically the mathematical operators T_{ij} called *transforms* are defined which allow the simple conversion from one coordinate system into the next. In processing step IV (Table 13; Fig. 5d to e) the exact mounting of the sensor within the aircraft and the actual positioning of the aircraft are determined.

The parameters that define T_{sp}, i.e., the transformation from the sensor to the platform reference frame, are the location and orientation of the payload sensor within X_p. Within the sensor installation (Sect. 2.3) these parameters were only known with moderate uncertainties ($\pm$ 0.5 m and $\pm$ 3°, respectively). Assuming that the position and attitude sensors of the Polar 5 operate on much higher precision, the other two transforms T_{pc} and T_{cg} are much more precise. The overall precision is thus limited by T_{sp}. To get the precise sensor installation parameters, a calibration routine is developed. The calibration is performed over calm ocean or shallow sea ice in order to get a sharp discontinuity of the surface echo. Furthermore clouds shouldn't be too thick, so that the surface return of the radar is the strongest signal of the profile. The calibration assumes that the altitude of the signal maximum is the surface reflectivity return, which is at an altitude of 0 m. Due to variations in position and attitude of the platform, this is extremely unlikely to happen consistently when using wrong parameters.

A suitable time interval of 2.5 h over calm ocean surface is considered and the downhill-simplex algorithm of Nelder and Mead (1965) is applied. The algorithm is used to minimize the cost function $c = \sum_i \zeta_i^2$. This yields the position and attitude of the payload sensor relative to X_p. ζ_i is the altitude (in X_g) of the signal maximum at time step i and c is ideally equal to 0. However in practice, the minimum reachable value is bounded by the finite width of the sensor's range gates. Using this calibration, c can be improved by a factor of three. Especially the attitude of the payload sensor has a large impact on the transformed target altitude. Using the same technique, offsets in the interpretation of time readings between the payload, position, and sensors attitude are detected in fractions of a second. These offsets affects c because T_{pc} and T_{cg} are time dependent.

The performed calibration of the $z_s^{(p)}$ coordinate of the sensor position, the sensor attitude and the time offsets technique is stable with respect to changes of the first guess in a domain of reasonable estimates and the time interval chosen for the calibration. The parameters $x_s^{(p)}$ and $y_s^{(p)}$ show only very little effect on c. This is expected since most of the time they are close to orthogonal with respect to zenith. When including them in the calibration, the algorithm still converged in all investigated cases, but much slower.

Finally, the last processing step V (Table 13) shows the result of the remapping that interpolates the data onto a constant vertical grid. Herein the time shift of the tilted profile to a true vertical column is considered allowing an easy combination with the nadir pointing MiRAC-P, lidar and radiation data. The processed reflectivity data product is publicly available (Kliesch and Mech, 2019).

4 Case study

One of the objectives of the ACLOUD campaign is the evaluation of satellite products in the Arctic (Wendisch et al., 2018). Here, the added value of airborne radar observations is highlighted in this example of a CloudSat underflight that took place over the Arctic ocean northwest of Svalbard (Fig. 4). A roughly 30 min flight leg centered around the exact overpass time at 10:27 at 78.925°N and 2.641°E is shown in Fig. 7 together with the corresponding CloudSat measurements. Note that this stretch is also included in the processing example of Fig. 5 which allows a more detailed look into the MiRAC radar measurements which provides more than a factor of ten finer vertical resolution (< 30 m) compared to CloudSats 250 m data product. Note, that the resolution associated with the CloudSat pulse length is 485 m (Stephens et al., 2009). In terms of spatial resolution the 1.4 (1.8) km cross-track (along track) of CloudSat roughly corresponds to 30 MiRAC measurements (15 depending on aircraft speed).

The measurements are taken from a leg when the Polar 5 was flying south-east passing through the marginal sea ice zone towards the open ocean which is reached roughly at 78.6 °N as indicated by the sea ice product derived from the Advanced Microwave Scanning Radiometer (AMSR2) by the University of Bremen (Spreen et al., 2008). The transition from 100 % sea

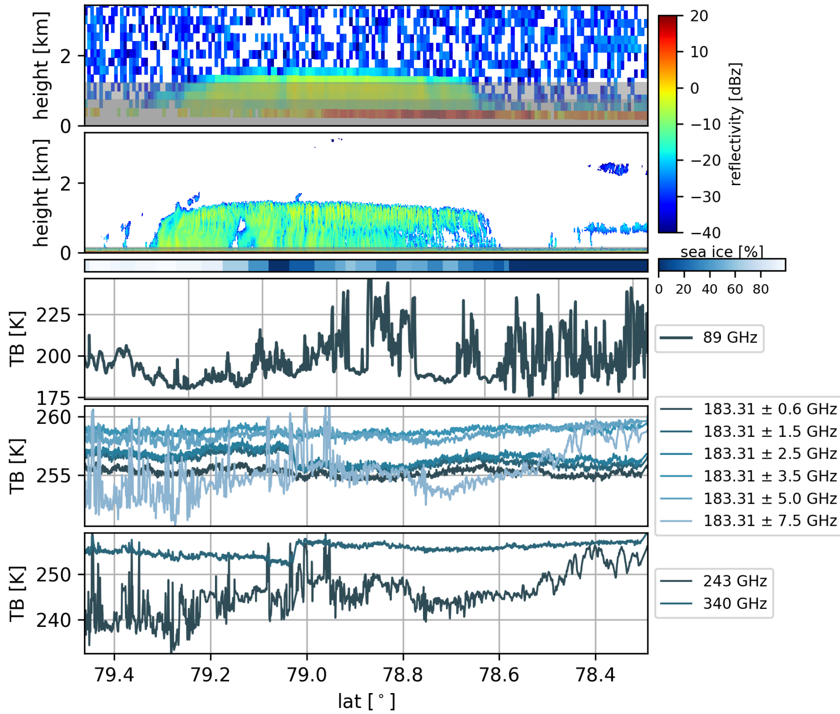

Figure 7. Vertical cross section of Z_e measured by CloudSat CPR (top) and the MiRAC radar on Polar 5 (second row) for the satellite underflight on May 27 2017 between 10:06 and 10:44 UTC along the black dashed line in Fig. 4. Grey shaded areas define the zone of reduced sensitivity. The third row gives the sea ice coverage ~~base~~ based on AMSR2 observations along the flight track. Row four to six show the passive radiometer measurements at 89 GHz ~~(ch 0)~~ from MiRAC-A and those channels of MiRAC-P, i.e., the six channels along the 183.31 GHz water vapor absorption line~~(Ch 1-6)~~, and the two channels at 243 and 340 GHz~~(Ch 7 and 8)~~.

ice fraction in the beginning of the flight leg to open ocean at the end of the track is nicely seen by the change in the radar surface return which significantly increases in the vertical pointing CPR measurements close to the surface (Fig. 7). Note that here the surface contaminated range gates, i.e. blind zone, have not been eliminated. For MiRAC the lowest 150 m need to be omitted while for CloudSat the nominal blind zone is about 0.75 to 1.25 km depending on the surface echo strength (Tanelli et al., 2008). Nevertheless, the CPR detects the precipitating cloud system with maximum cloud top height of 1.6 km rather consistent in its spatial extent of (150 km) with MiRAC. In terms of reflectivity the CPR indicates slightly higher average values especially in the more southern part over ocean which however might result from additional surface contamination. Due to the low cloud top height we retain from looking at height averaged Z_e profiles as done by (Delanoë et al., 2013) for the case of a 5 km high nimbostratus cloud. As shown in Fig. 5 MiRAC is able to resolve the individual patches of enhanced reflectivities associated with turbulent processes as well as smaller scale clouds. Additional underflights were performed with CloudSat during ACLOUD unfortunately no CPR measurements are available due to satellite problems.

The daily AMSR2 sea ice product with 6.25 km spatial resolution mainly relies on TB measurements at 89 GHz. Such measurements are available with much finer resolution from MiRAC-A's passive 89 GHz channel. As can be seen in the beginning of the flight track strong fluctuations in this channel between roughly 190 and 240 K mirror a strong change in surface emissivity (Fig. 7) with the lowest values being consistent with open water while higher TB indicate ice. These high frequency fluctuations are consistent with visual observations which reveal a high degree of brokenness in the sea ice. Towards the end TB stay at lower values typical for ocean surfaces before they increase again, however, with much smoother behaviour than during the broken sea ice conditions. This increase can be attributed to liquid water emission by the thin ($dz = 350$m) cloud shown by the radar in roughly 800 m height which can not be resolved by the CPR.

Time series of MiRAC-P TB clearly identify optically thick channels which are not affected by the surface by their relatively constant behaviour during the complete flight leg (Fig. 7). The first channel at 183±0.6 GHz being closest to the strong water vapor absorption shows the coldest TB as its emission stems from water vapor at higher altitudes. With channels moving farther away from the line center channels receive successively radiation from lower layers as the emission stems from lower atmospheric layers. At a certain point along the line the atmosphere becomes transparent and surface emission also contributes to TB. This can be best seen for the outermost 183±7.5 GHz and the window channel at 243 GHz. This channel is of particular interest as it will also be flown on the Ice Cloud Imager (ICI; Kangas et al., 2014) onboard of MetOP-SG to be launched in 2023. Scattering by ice particles strongly increases with increasing frequency and therefore a brightness temperature depression can occur. Disentangling the contribution of water vapor, liquid water, the surface and ice scattering is complex and is part of the ongoing retrieval development.

5 Cloud statistics

MiRAC as a remote sensing suite has been operated on Polar 5 during ACLOUD on 19 research flights ~~which sums~~ summing up to more than 80 flight hours. In a first analysis macroscopic cloud properties are derived for the ~~full~~ whole flight campaign. For that purpose the processed reflectivities (Sect. 3) ~~taken in~~ measured from flight altitudes of at least ~~2300 m~~ 2300 m and with small aircraft ~~orientation~~ pitch and role angles ($\epsilon < 10°$ ~~,~~ and $|\rho| < 3°$, respectively) are considered~~, resulting in usable~~. This results in 52 % of the total flight time along the tracks shown in Fig. 4 ~~. No measurements above land, i.e., the strong~~ being usable for the analysis. Due to the orography of Svalbard, ~~are included. As seen~~ radar measurements are difficult to interpret. Therefore, measurements over land are excluded. Most of the time Polar 5 was flying in an altitude of about 2900 to 3000 m, which can be seen as well in Fig. 8 where about 80 % of all measurements considered in the statistical analysis ~~have been acquired with flight altitude above .~~ were acquired with this flight altitude or above. Figure 8 and Table 15 as well show, that about 57 % of the measurements were taken over open ocean and 43 % over sea ice. It has to be kept in mind, that flight patterns were planed to observe clouds according to numerical weather prediction models. Therefore, the statistics might be biased.

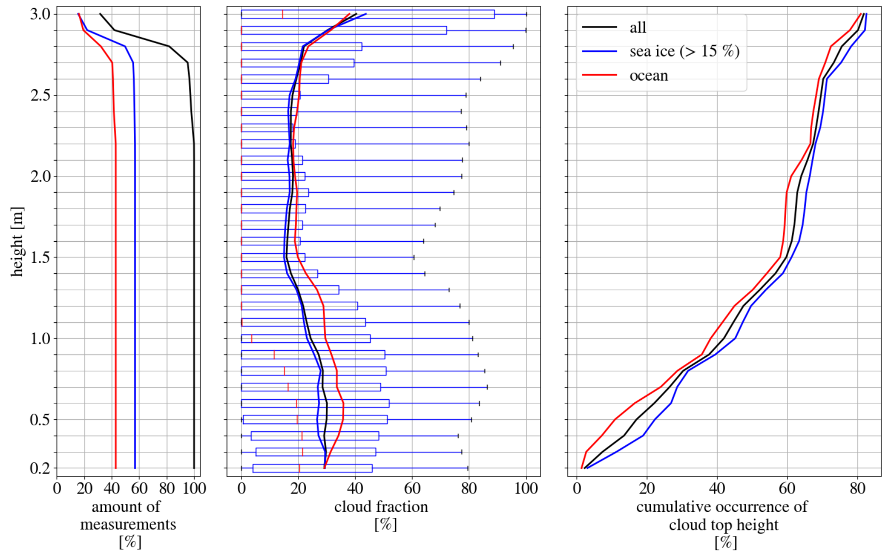

Figure 8. Height dependent cloud top height and cloud fraction (CF) on intervals of 100 m. The interval center is written in the y-ordinate~~:~~ ~~left~~. Left: number of measurements, center: solid lines describe the total averaged cloud fraction in each height over all profiles; box-whisker ~~plot~~ plots of ~~20-min-CF~~ cloud fraction averaged over 20 min with percentiles of 10, 25, 50, 75, and 90 % from left to right, respectively~~.~~ ~~The solid lines describe the total averaged cloud fraction~~, right: cumulative occurrence of averaged cloud top height. The sea ice fraction is derived from satellite observations by AMSR2.

A radar cloud mask is defined by considering profiles of Z_e. A profile is attributed to be cloudy if a signal greater than Z_{min} (Fig. 1) reaches a ~~greater vertical extent~~ vertical extent of more than 25 m, which roughly ~~correspond~~ corresponds to two range gates ~~in comparison to Table 11~~for chirp table III (or one for chirp I and II, see Table 11). The cloud mask is then reduced to a one dimensional vector along the flight track of ones and zeros describing clouds and clear sky, respectively. During the ACLOUD field campaign clouds occurred in 75 % of the flight time (Table 15)~~which, however, has to be interpreted with care as flight patterns were selected to investigate clouds~~, with 80 % over ocean and 72 % over sea ice. Figure 8 provides the ~~vertical cloud fraction~~ cloud fraction vertically resolved in 100 m intervals. ~~It is highest~~ The highest values are present in the lowest 1000 m with about 25 to 30 % ~~and at heights above . The latter results from cloud tops exceeding the typical flight level of . In that cases the aircraft is~~ over sea ice and 30 % over ocean (solid lines in Fig. 8). The cloud fraction is in general slightly higher over ocean than over sea ice in all heights. For measurements at higher levels (above 2850 m) the cloud fraction increases which is most likely an artefact since measurements at higher levels were only taken when Polar 5 was forced to climb ~~up, to get cloud profiles of the entire cloud. Figure 8 shows that about of the measurements were taken at altitudes higher than~~ above clouds due to cloud tops exceeding the typical flight level of 10000 ft.

In order to characterize the cloud variability within the grid cell of a global climate model, cloud fraction is calculated for 20 min legs. With a typical flight speed of 80 m/s this corresponds to roughly 100 km. The resulting distribution of cloud

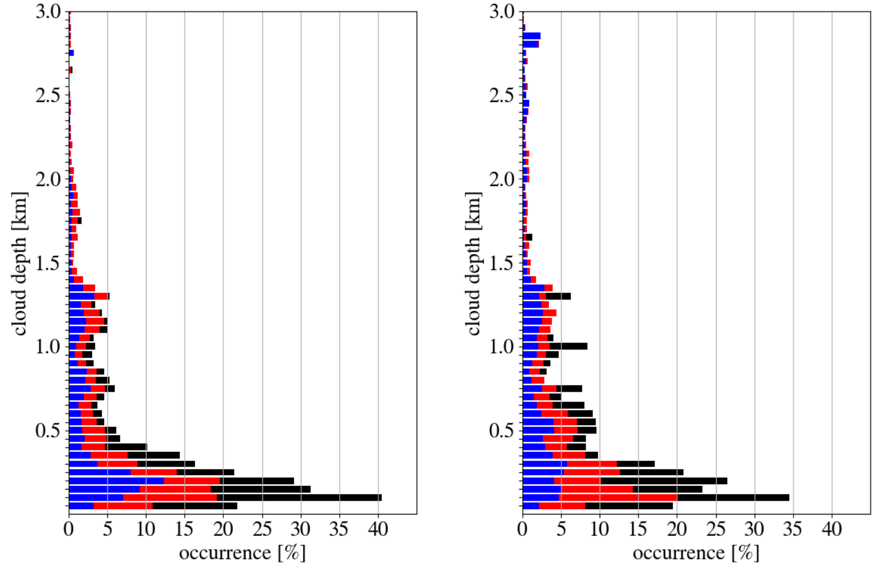

Figure 9. Cloud depth of ~~different layered~~ single- and multi-layer clouds. Blue describes the cloud depth distribution of all ~~one layer~~ single-layer clouds~~;~~, red ~~describes all cloud~~ for depths of ~~two layer~~ clouds ~~, that is, the~~ with two layers~~results in two cloud depth values;~~, and black describes all cloud depths of clouds with ~~more than~~ three and more layers. For multi-layer clouds the cloud depth of each layer is counted. The data are normalized such that all thickness bins of one type add up to 100 %. Left: sea ice surface (> 15 %), right: ocean surface.

fraction for each height is shown in Fig. 8 in the form of box plots. Again highest variability with an interquartile range of 40 % or more occur in the lowest 500 to 1000 m above ground level associated with low clouds and above 3 km due to the sampling. The radar signal is dominated by larger particles and therefore even few precipitating snow particles cause significant Z_e. Therefore, the averaged cloud fraction in the lowest altitudes amounting to roughly 30 % is likely due to snow precipitation. Interestingly, below 500 m the spread in cloud fraction is decreasing towards the ground indicating the spatially rather constant occurrence of snow precipitation.

The radar cloud mask was used to derive information on cloud boundaries. This revealed that about 40 % of all clouds show cloud tops below 1000 m (Fig. 8) which are therefore likely to be missed by CloudSat. 60 % of the cloud tops can be found below 1500 m. Throughout the observed 3000 m, the cloud tops over ocean are higher than the one over sea ice. When looking at the vertical structure of clouds 62 (35) % appear to be single (two) layer clouds (Table 15) and even three or more layers are identified about three percent of the time. Looking at the thickness of these layer, not surprisingly, the multi-layer clouds show the shortest vertical extent (median $\Delta z = 205$ m) (Fig. 9). Over ice, there are almost no clouds which have vertical extents larger than 2000 m. Most clouds have thicknesses below 1200 m which is consistent with the most frequent cloud top heights (Fig. 8) and the frequent occurrence of precipitating clouds classical for arctic mixed-phase stratiform clouds. As discussed in

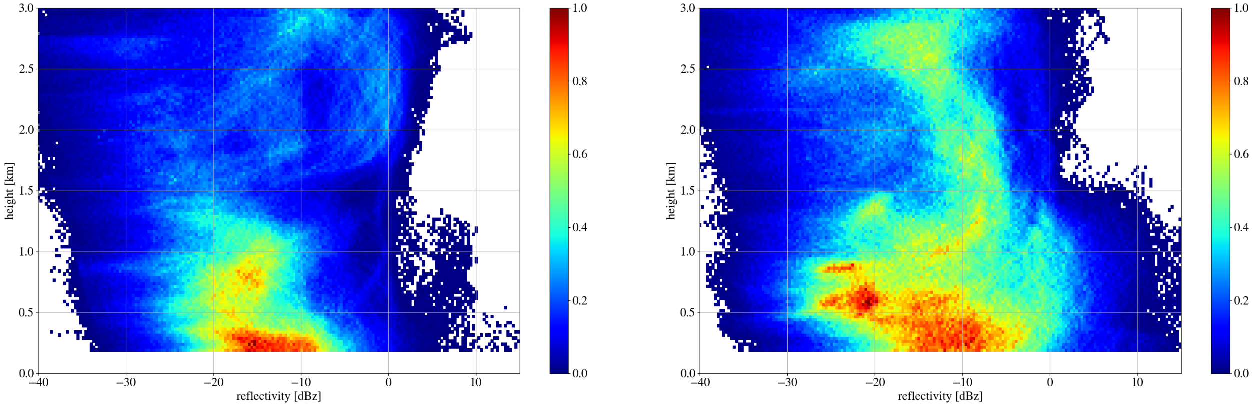

Figure 10. Contour Frequency by Altitude Diagrams CFADs of sea ice (left) and ocean (right). The frequency is normalized by the highest number within the CFADs for each case, respectively. A sea ice fraction of > 15 % is used (AMSR2).

Sect. 4 the information on liquid water from the passive channels can be used over open ocean to determine the LWP. In this way, together with AMALi and radiation measurements, detailed insights into mixed phase clouds will be gained.

In the beginning of the ACLOUD campaign a cold air outbreak could be observed which showed the classical behaviour of a thickening boundary layer with higher cloud top heights when transitioning from the sea ice to the open ocean. During the Aerosol-Cloud Coupling And Climate Interactions in the Arctic (ACCACIA) campaign Young et al. (2016) investigated the microphysical structure of clouds during such a cold air outbreak and found largest number concentrations of liquid droplets over sea ice decreasing towards the ocean while ice characteristics did not change significantly. In a first statistical attempt all profiles observed during ACLOUD were separated into ocean and sea ice surface conditions using the AMSR2 sea ice concentration ~~of Bremen~~ and a threshold of 15 %. The number of measurements above sea ice and broken sea ice is ~~increased with respect to~~ higher than the number of measurements ~~above~~ over open ocean (Fig. 8). Figure 8 additionally shows less clouds above sea ice, which most frequently occur below 800 m. ~~This is supported by Fig. 9, in which cloud thickness over sea ice is mostly lower than 800 m.~~

After analyzing the macrophysical properties, Constant Frequency by Altitude Diagrams (CFADs; Yuter and Houze, 2002) will now be considered, which provide the frequency of occurrence of Z_e over the vertical profile. Figure 10 clearly shows the much lower vertical extent of clouds over sea ice. The highest frequency for Z_e occurs below 400 m between -20 and -10 dBz indicating more frequent, but rather low amounts of precipitation. A second cluster with lower amount can be found between 500 and 1000 m with Z_e values between -20 and -15 dBz. Some higher reflectivities around 0 dBz can be between 2 and 3 km. In contrast measurements over open ocean show higher concentration of reflectivities in the lowest levels between -15 and -8 dBz up to 500 m and a secondary peak of clouds clustering -25 and -20 dBz between 500 and 900 m. This second peak not visible over sea ice corresponds to the elevated Arctic boundary layer height and the cloud forming here (Chechin and Lüpkes, 2019). A band spanning from around -10 dBz in ~~altitudes between 1 and~~ 1 km to -18 dBz at 3 km belongs to the vertical extending clouds over ocean. In general radar reflectivities are rather low with only few measurement over ocean showing higher reflectivities than 0 dBz and almost none over ice emphasizing the need for a highly sensitive radar to observe Arctic low level clouds.

6 Conclusions and Outlook

The MiRAC is a novel airborne, active and passive microwave remote sensing instrument package with a 94 GHz FMCW radar and radiometers between 89 and 340 GHz. The instrument has been tailored to be fit into the Polar 5 aircraft and successfully participated in the ACLOUD campaign (Wendisch et al., 2018). A procedure to filter radar side-lobes and to provide geo-referenced data to the community has been developed. The preliminary data analysis from ACLOUD clearly demonstrates the capabilities of MiRAC especially for the study of low-level, mixed-phase Arctic clouds.

Deriving cloud microphysical properties from MiRAC and especially in synergy with other instruments, e.g., the AMALi lidar, operated on the Polar 5 will be the next step. As illustrated the passive channels are highly sensitive to sea ice allowing to determine the occurrence of sea ice with high spatial resolution. This, however, limits the possibility to retrieve cloud liquid water to open ocean. Exploring the information especially from the high frequency channels is of special interest in light of the upcoming MetOP-SG Ice Cloud Imager.

The Doppler spectra acquired by the MiRAC radar are difficult to interpret due to the influence of the aircraft motion on the Doppler shifts. Attempts to correct this are ongoing. Furthermore, information about multi-mode behaviour in the spectra can also be used to better interpret the microphysics especially for those flights where in-situ measurements from the Polar 6 were performed.

During March/April 2019 MiRAC was part of the installation on Polar 5 in the Joint Aircraft campaign observing FLUXes of energy and momentum in the cloudy boundary layer over polar sea ice and ocean (AFLUX) flying out Longyearbyen on Svalbard. In September 2019 the Multidisciplinary drifting Observatory for the Study of Arctic Climate (MOSAiC) campaign (http://www.mosaic-expedition.org) will start. MiRAC-P will be operated in up-looking geometry on board the research vessel Polarstern to infer moisture profiles in the central Arctic. In March/April and August/September 2020 flights with MiRAC-A and a downward looking Humidity And Temperature PROfiler (HATPRO; Rose et al., 2005) on board the Polar 5 aircraft will be performed again from Svalbard to further infer cloud characteristics in different seasons.

Appendix A: Coordinate transformation

First the mathematical basis of the coordinate transformation and the application to the experiment geometry followed by explicit coordinate transforms between the different reference frames discussed in Sect. 3 is provided.

A1 Mathematical basis

For the transition from one reference frame X_i to another X_j a mathematical operator T_{ij} called *transform* is introduced. It acts upon a position vector $\boldsymbol{r}^{(i)}$ in X_i-coordinates and returns its coordinates $\boldsymbol{r}^{(j)}$ in X_j:

$$\boldsymbol{r}^{(j)} = T_{ij}(\boldsymbol{r}^{(i)}). \tag{A1}$$

The vector is first rotated, then shifted:

$$T_{ij}(\boldsymbol{r}^{(i)}) = R_{ij} \cdot \boldsymbol{r}^{(i)} + \boldsymbol{S}_{ij}, \tag{A2}$$

where R_{ij} is a matrix expressing the rotation of X_i relative to X_j, $\boldsymbol{S}_{ij}$ is the position of X_i in coordinates of X_j and $\cdot$ is the matrix product.

The inverse of the transform is obtained by solving Eq. (A2) for $\boldsymbol{r}^{(i)}$:

$$T_{ji}(\boldsymbol{r}^{(j)}) = R_{ij}^{-1} \cdot \boldsymbol{r}^{(j)} - R_{ij}^{-1} \cdot \boldsymbol{S}_{ij}, \tag{A3}$$

with $^{-1}$ being the matrix inversion operator (the inverse of a rotation matrix can be easily obtained by transposition). Equation (A3) has the same form as Eq. (A2), with rotation $R_{ji} = R_{ij}^{-1}$ and shift $\boldsymbol{S}_{ji} = \left(-R_{ij}^{-1} \cdot \boldsymbol{S}_{ij}\right)$.

The composition of two transforms T_{ij} (from X_i to X_j) and T_{jk} (from X_j further to X_k) yields the direct transform from X_i to X_k. It is obtained by applying T_{jk} to the result of T_{ij}:

$$T_{ik}(\boldsymbol{r}^{(i)}) = (R_{jk} \cdot R_{ij}) \cdot \boldsymbol{r}^{(i)} + (R_{jk} \cdot \boldsymbol{S}_{ij} + \boldsymbol{S}_{jk}), \tag{A4}$$

where $R_{ik} = (R_{jk} \cdot R_{ij})$ and $\boldsymbol{S}_{ik} = (R_{jk} \cdot \boldsymbol{S}_{ij} + \boldsymbol{S}_{jk})$ can be identified, respectively, as the rotation and shift of the composed transform.

A2 Application to the experiment geometry

Once the three base transforms connecting the four reference frames X_s, X_p, X_c, and X_g are established, the coordinates of the measurement targets can be transformed from X_s to X_g by applying the transform

$$T_{sg} = T_{cg} \circ T_{pc} \circ T_{sp} \tag{A5}$$

to the position vector $\boldsymbol{r}^{(s)}$ of the measurement (since measurements are only performed along the $y^{(s)}$-axis, $\boldsymbol{r}^{(s)} = r \cdot \boldsymbol{e}_y$) the transforms are obtained in principle.

The transform T_{sp} from X_s to X_p is independent of time. It is described by the location of the payload sensor relative to the position sensor and by the orientation of the payload sensor relative to the sensor attitude. These relations are known from surveys before the campaign.

The time-dependent transform T_{pc} from X_p to X_c is purely rotational as the two reference frames are co-located. It is described by the three principal rotation angles of the platform (Fig. 6). To reach X_p from X_c, the coordinate system is first rotated by the (true) heading η (distance to north) about the z-axis in mathematically negative sense. Then, a rotation about the x-axis by the pitch angle ϵ is applied (elevation of the nose). Finally, the system is rotated about the y-axis by the roll angle ρ. These three angles are recorded by the attitude sensor, which in practice is an inertial navigation system (INS) on board the aircraft.

The transform T_{cg} from X_c to X_g (λ, ϕ, h) is time-dependent, too. It is done with knowledge of the platform position relative to the planet which is recorded by the position sensor (e.g., by use of a radio navigation-satellite service such as GPS). Since X_c is aligned with the local east, north, and zenith, both shift and rotation of T_{cg} are determined by the platform position.

A3 From X_s to X_p

The shift part of T_{sp} is the sensor position in X_s coordinates:

$$\boldsymbol{S}_{sp} = \boldsymbol{r}_s^{(p)}. \tag{A6}$$

As the $x^{(s)}$- and $z^{(s)}$-axes are undefined, the rotation is sufficiently described by two angles: The azimuth angle $\alpha_s^{(p)}$ measures how far the payload sensor's line of sight is rotated about the platform's $z^{(p)}$-axis away from the forward direction ($y^{(p)}$-axis); it is measured in mathematically negative sense (forward-right-backward-left). The view angle $\beta_s^{(p)}$ is the distance to the negative $z^{(p)}$-axis (i.e., zero if looking downward w.r.t. the platform reference frame). The rotational part of T_{sp} is the successive application of these two rotations:

$$R_{sp} = R_{sp,\alpha} \cdot R_{sp,\beta}, \tag{A7}$$

with

$$R_{sp,\alpha} = \begin{pmatrix} \cos\alpha_s^{(p)} & \sin\alpha_s^{(p)} & 0 \\ -\sin\alpha_s^{(p)} & \cos\alpha_s^{(p)} & 0 \\ 0 & 0 & 1 \end{pmatrix} \tag{A8}$$

$$R_{sp,\beta} = \begin{pmatrix} 1 & 0 & 0 \\ 0 & \sin\beta_s^{(p)} & \cos\beta_s^{(p)} \\ 0 & -\cos\beta_s^{(p)} & \sin\beta_s^{(p)} \end{pmatrix} \tag{A9}$$

A4 From X_p to X_c

Since the origins of the two reference frames are identical, this transform is purely rotational. The platform attitude relative to X_c is described by the angles η, ϵ, and ρ (Sect. 3.2, the superscript ${}^{(c)}$ is omitted here). The transition from X_p to X_c is achieved by successively reversing these rotations:

$$R_{pc} = R_{pc,\eta} \cdot R_{pc,\epsilon} \cdot R_{pc,\rho}, \tag{A10}$$

with

$$R_{pc,\eta} = \begin{pmatrix} \cos\eta & \sin\eta & 0 \\ -\sin\eta & \cos\eta & 0 \\ 0 & 0 & 1 \end{pmatrix} \tag{A11}$$

$$R_{sp,\epsilon} = \begin{pmatrix} 1 & 0 & 0 \\ 0 & \cos\epsilon & -\sin\epsilon \\ 0 & \sin\epsilon & \cos\epsilon \end{pmatrix} \tag{A12}$$

$$R_{sp,\rho} = \begin{pmatrix} \cos\rho & 0 & \sin\rho \\ 0 & 1 & 0 \\ -\sin\rho & 0 & \cos\rho \end{pmatrix} \tag{A13}$$

A5 From $\boldsymbol{X_c}$ to $\boldsymbol{X_g}$

Here, the platform position is used. It is usually recorded in the spherical coordinates longitude λ_c, latitude ϕ_c, and altitude h_c above mean sea level (superscript $^{(g)}$ is omitted here). Note that, because the origins of X_c and X_p coincide, $\lambda^{(c)} = \lambda^{(p)}$, $\phi^{(c)} = \phi^{(p)}$ and $h^{(c)} = h^{(p)}$. They sufficiently describe both the shift and the rotation of T_{cg}. The shift part of T_{cg} is the platform position within X_g:

$$\boldsymbol{S}_{cg} = (x_c^{g)}, y_c^{(g)}, z_c^{(g)}), \tag{A14}$$

where $(x_c^{(g)}, y_c^{(g)}, z_c^{(g)})$ is the Cartesian representation of (λ_c, ϕ_c, h_c). The rotation matrix is established by first accounting for the latitude, then for the longitude:

$$R_{cg} = R_{cg,\lambda} \cdot R_{cg,\phi}, \tag{A15}$$

with

$$R_{cg,\lambda} = \begin{pmatrix} -\sin\lambda_c & \cos\lambda_c & 0 \\ \cos\lambda_c & \sin\lambda_c & 0 \\ 0 & 0 & 1 \end{pmatrix} \tag{A16}$$

$$R_{cg,\phi} = \begin{pmatrix} 1 & 0 & 0 \\ 0 & \sin\phi_c & -\cos\phi_c \\ 0 & \cos\phi_c & \sin\phi_c \end{pmatrix} \tag{A17}$$

A6 From X_s to X_g

A transform directly from X_s to X_g can be obtained by use of the composition formula in Eq. (A4):

$$T_{sg} = T_{cg} \circ T_{pc} \circ T_{sp}. \tag{A18}$$

This is conveniently done by a computing machine. The explicit form of T_{sg} is not derived .

In order to obtain the target coordinates in spherical representation, the position vector in X_g is eventually re-converted to spherical coordinates after application of the transform.

Data availability. MiRAC-A radar reflectivity and brightness temperature data are available at PANGAEA database (https://doi.pangaea.de/10.1594/PANGAEA.899565).

Author contributions. SC conceptionalized MiRAC and initiated the DFG MiRAC and B03 project. TR designed and built MiRAC. MM organized all aspects of the aircraft integration and operation as well as the data analysis. PK advised on radar integration and processing. AA developed the coordination transformation. LK developed the filtering procedure and conducted the statistical analysis. All co-authors contributed to writing the paper.

Competing interests. The authors declare that they have no conflict of interest.

Acknowledgements. MiRAC was acquried via grant INST 268/331-1 of the Deutsche Forschungsgemeinschaft (DFG, German Research Foundation). We gratefully acknowledge the funding by the DFG - project number 268020496 - TRR 172 “ArctiC Amplification: Climate Relevant Atmospheric and SurfaCe Processes, and Feedback Mechanisms $(AC)^3$” in sub-project “B03: Characterization of Arctic mixed-phase clouds by airborne in-situ measurements and remote sensing“. We thank the Alfred Wegener Institute for the support with the installation and operation of MiRAC on Polar 5. We thank Birte Kulla for her support preparing the manuscript.

References

Andronache, C.: Characterization of Mixed-Phase Clouds: Contributions From the Field Campaigns and Ground Based Networks, in: Mixed-Phase Clouds: Observations and Modeling, edited by Andronache, C., pp. 97–120, Elsevier, https://doi.org/10.1016/B978-0-12-810549-8.00005-2, http://www.sciencedirect.com/science/article/pii/B9780128105498000052, 2017.

Burns, D., Kollias, P., Tatarevic, A., Battaglia, A., and Tanelli, S.: The performance of the EarthCARE cloud profiling radar in marine stratiform clouds, Journal of Geophysical Research, 121, 14 525–14 537, https://doi.org/10.1002/2016JD025090, https://agupubs.onlinelibrary.wiley.com/doi/abs/10.1002/2016JD025090, 2016.

Chechin, D. G. and Lüpkes, C.: Baroclinic low-level jets in Arctic marine cold-air outbreaks, IOP Conference Series: Earth and Environmental Science, 231, 012 011, https://doi.org/10.1088/1755-1315/231/1/012011, http://stacks.iop.org/1755-1315/231/i=1/a=012011?key=crossref.185649e646edcbc0155809fcb2c33530, 2019.

Curry, J. A., Schramm, J. L., Rossow, W. B., and Randall, D.: Overview of Arctic Cloud and Radiation Characteristics, Journal of Climate, 9, 1731–1764, https://doi.org/10.1175/1520-0442(1996)009<1731:ooacar>2.0.co;2, 2002.

Delanoë, J., Protat, A., Vinson, J.-P., Fontaine, E., Schwarzenboeck, A., and Flamant, C.: RASTA: The airborne cloud radar, a tool for studying cloud and precipitation during HyMeX SOP1.1., in: 6th HyMeX Workshop, Primosten, Croatia, https://hal.archives-ouvertes.fr/hal-00713364, 2012.

Delanoë, J., Protat, A., Jourdan, O., Pelon, J., Papazzoni, M., Dupuy, R., Gayet, J. F., and Jouan, C.: Comparison of airborne in situ, airborne radar-lidar, and spaceborne radar-lidar retrievals of polar ice cloud properties sampled during the POLARCAT campaign, Journal of Atmospheric and Oceanic Technology, 30, 57–73, https://doi.org/10.1175/JTECH-D-11-00200.1, https://journals.ametsoc.org/doi/full/10.1175/JTECH-D-11-00200.1, 2013.

Fang, M., Albrecht, B., Jung, E., Kollias, P., Jonsson, H., and PopStefanija, I.: Retrieval of vertical air motion in precipitating clouds using mie scattering and comparison with in situ measurements, Journal of Applied Meteorology and Climatology, 56, 537–553, https://doi.org/10.1175/JAMC-D-16-0158.1, https://journals.ametsoc.org/doi/10.1175/JAMC-D-16-0158.1, 2017.

Graversen, R. G., Mauritsen, T., Tjernström, M., Källén, E., and Svensson, G.: Vertical structure of recent Arctic warming, Nature, 451, 53–56, https://doi.org/10.1038/nature06502, http://www.nature.com/articles/nature06502, 2008.

Kangas, V., D'Addio, S., Klein, U., Loiselet, M., Mason, G., Orlhac, J. C., Gonzalez, R., Bergada, M., Brandt, M., and Thomas, B.: Ice cloud imager instrument for MetOp Second Generation, in: 13th Specialist Meeting on Microwave Radiometry and Remote Sensing of the Environment, MicroRad 2014 - Proceedings, pp. 228–231, https://doi.org/10.1109/MicroRad.2014.6878946, 2014.

Khanal, S. and Wang, Z.: Evaluation of the lidar-radar cloud ice water content retrievals using collocated in situ measurements, Journal of Applied Meteorology and Climatology, 54, 2087–2097, https://doi.org/10.1175/JAMC-D-15-0040.1, https://journals.ametsoc.org/doi/10.1175/JAMC-D-15-0040.1, 2015.

Kliesch, L.-L. and Mech, M.: Airborne radar reflectivity and brightness temperature measurements with POLAR 5 during ACLOUD in May and June 2017, https://doi.pangaea.de/10.1594/PANGAEA.899565, 2019.

Knudsen, E. M., Heinold, B., Dahlke, S., Bozem, H., Crewell, S., Gorodetskaya, I. V., Heygster, G., Kunkel, D., Maturilli, M., Mech, M., Viceto, C., Rinke, A., Schmithüsen, H., Ehrlich, A., MacKe, A., Lüpkes, C., and Wendisch, M.: Meteorological conditions during the ACLOUD/PASCAL field campaign near Svalbard in early summer 2017, Atmospheric Chemistry and Physics, 18, 17 995–18 022, https://doi.org/10.5194/acp-18-17995-2018, https://www.atmos-chem-phys.net/18/17995/2018/, 2018.

Küchler, N., Kneifel, S., Löhnert, U., Kollias, P., Czekala, H., and Rose, T.: A W-band radar-radiometer system for accurate and continuous monitoring of clouds and precipitation, Journal of Atmospheric and Oceanic Technology, 34, 2375–2392, https://doi.org/10.1175/JTECH-D-17-0019.1, https://journals.ametsoc.org/doi/abs/10.1175/JTECH-D-17-0019.1, 2017.

Lee, J. S., Jurkevich, I., Dewaele, P., Wambacq, P., and Oosterlinck, A.: Speckle filtering of synthetic aperture radar images: a review, Remote Sensing Reviews, 8, 313–340, https://doi.org/10.1080/02757259409532206, https://doi.org/10.1080/02757259409532206, 1994a.

Lee, W.-C., Dodge, P., Marks, F. D., Hildebrand, P. H., Lee, W.-C., Dodge, P., Jr., F. D. M., and Hildebrand, P. H.: Mapping of Airborne Doppler Radar Data, Journal of Atmospheric and Oceanic Technology, 11, 572–578, https://doi.org/10.1175/1520-0426(1994)011<0572:MOADRD>2.0.CO;2, http://journals.ametsoc.org/doi/abs/10.1175/1520-0426{%}281994{%}29011{%}3C0572{%}3AMOADRD{%}3E2.0.CO{%}3B2, 1994b.

Li, L., Heymsfield, G. M., Tian, L., and Racette, P. E.: Measurements of ocean surface backscattering using an airborne 94-GHz cloud radar - Implication for calibration of airborne and spaceborne w-band radars, Journal of Atmospheric and Oceanic Technology, 22, 1033–1045, https://doi.org/10.1175/JTECH1722.1, 2005.

Maahn, M., Burgard, C., Crewell, S., Gorodetskaya, I. V., Kneifel, S., Lhermitte, S., Van Tricht, K., and Van Lipzig, N. P.: How does the spaceborne radar blind zone affect derived surface snowfall statistics in polar regions?, Journal of Geophysical Research, 119, 13,604–13,620, https://doi.org/10.1002/2014JD022079, http://onlinelibrary.wiley.com/doi/10.1002/2014JD022079/abstract, 2014.

Mech, M., Orlandi, E., Crewell, S., Ament, F., Hirsch, L., Hagen, M., Peters, G., and Stevens, B.: HAMP-the microwave package on the high altitude and long range research aircraft (HALO), Atmospheric Measurement Techniques, 7, 4539–4553, https://doi.org/10.5194/amt-7-4539-2014, 2014.

Mioche, G., Jourdan, O., Ceccaldi, M., and Delanoë, J.: Variability of mixed-phase clouds in the Arctic with a focus on the Svalbard region: A study based on spaceborne active remote sensing, Atmospheric Chemistry and Physics, 15, 2445–2461, https://doi.org/10.5194/acp-15-2445-2015, http://www.atmos-chem-phys.net/15/2445/2015/, 2015.

Morrison, H., De Boer, G., Feingold, G., Harrington, J., Shupe, M. D., and Sulia, K.: Resilience of persistent Arctic mixed-phase clouds, Nature Geoscience, 5, 11–17, https://doi.org/10.1038/ngeo1332, http://www.nature.com/ngeo/journal/v5/n1/full/ngeo1332.html, 2012.

Nelder, J. A. and Mead, R.: A Simplex Method for Function Minimization, The Computer Journal, 7, 308–313, https://doi.org/10.1093/comjnl/7.4.308, https://academic.oup.com/comjnl/article-lookup/doi/10.1093/comjnl/7.4.308, 1965.

Nomokonova, T., Ebell, K., Löhnert, U., Maturilli, M., Ritter, C., and O'Connor, E.: Statistics on clouds and their relation to thermodynamic conditions at Ny-Ålesund using ground-based sensor synergy, Atmospheric Chemistry and Physics Discussions, pp. 1–37, https://doi.org/10.5194/acp-2018-1144, https://www.atmos-chem-phys-discuss.net/acp-2018-1144/, 2018.

Osborne, E., Richter-Menge, J., and Jeffries, M.: Arctic Report Card 2018, Tech. rep., NOAA, https://www.arctic.noaa.gov/Report-Card, 2018.

Rauber, R. M., Ellis, S. M., Vivekanandan, J., Stith, J., Lee, W. C., McFarquhar, G. M., Jewett, B. F., and Janiszeski, A.: Finescale structure of a snowstorm over the northeastern United States: A first look at high-resolution hiaper cloud radar observations, Bulletin of the American Meteorological Society, 98, 253–269, https://doi.org/10.1175/BAMS-D-15-00180.1, http://journals.ametsoc.org/doi/10.1175/BAMS-D-15-00180.1, 2017.

Rose, T., Crewell, S., Löhnert, U., and Simmer, C.: A network suitable microwave radiometer for operational monitoring of the cloudy atmosphere, Atmospheric Research, 75, 183–200, https://doi.org/10.1016/j.atmosres.2004.12.005, http://www.sciencedirect.com/science/article/pii/S0169809505000189, 2005.

Schäfer, M., Bierwirth, E., Ehrlich, A., Jäkel, E., and Wendisch, M.: Airborne observations and simulations of three-dimensional radiative interactions between Arctic boundary layer clouds and ice floes, Atmospheric Chemistry and Physics, 15, 8147–8163, https://doi.org/10.5194/acp-15-8147-2015, https://www.atmos-chem-phys.net/15/8147/2015/, 2015.

Serreze, M. C., Barrett, A. P., Stroeve, J. C., Kindig, D. N., and Holland, M. M.: The emergence of surface-based Arctic amplification, The Cryosphere, 3, 11–19, 2009.

Shupe, M. D., Turner, D. D., Walden, V. P., Bennartz, R., Cadeddu, M. P., Castellani, B. B., Cox, C. J., Hudak, D. R., Kulie, M. S., Miller, N. B., Neely, R. R., Neff, W. D., Rowe, P. M., Shupe, M. D., Turner, D. D., Walden, V. P., Bennartz, R., Cadeddu, M. P., Castellani, B. B., Cox, C. J., Hudak, D. R., Kulie, M. S., Miller, N. B., Ryan R. Neely, I., Neff, W. D., and Rowe, P. M.: High and Dry: New Observations of Tropospheric and Cloud Properties above the Greenland Ice Sheet, Bulletin of the American Meteorological Society, 94, 169–186, https://doi.org/10.1175/BAMS-D-11-00249.1, http://journals.ametsoc.org/doi/abs/10.1175/BAMS-D-11-00249.1, 2013.

Shupe, M. D., Thieman, M. M., Turner, D. D., Mlawer, E. J., Shippert, T., and Zwink, A.: Deriving Arctic Cloud Microphysics at Barrow, Alaska: Algorithms, Results, and Radiative Closure, Journal of Applied Meteorology and Climatology, 54, 1675–1689, https://doi.org/10.1175/jamc-d-15-0054.1, https://journals.ametsoc.org/doi/10.1175/JAMC-D-15-0054.1, 2015.

Spreen, G., Kaleschke, L., and Heygster, G.: Sea ice remote sensing using AMSR-E 89-GHz channels, Journal of Geophysical Research: Oceans, 113, https://doi.org/10.1029/2005JC003384, https://agupubs.onlinelibrary.wiley.com/doi/full/10.1029/2005JC003384, 2008.

Stachlewska, I. S., Neuber, R., Lampert, A., Ritter, C., and Wehrle, G.: AMALi-the Airborne Mobile Aerosol Lidar for Arctic research, Atmospheric Chemistry and Physics, 10, 2947–2963, https://doi.org/10.5194/acp-10-2947-2010, https://www.atmos-chem-phys.net/10/2947/2010/, 2010.

Stephens, G. L., Vane, D. G., Tanelli, S., Im, E., Durden, S., Rokey, M., Reinke, D., Partain, P., Mace, G. G., Austin, R., L'Ecuyer, T., Haynes, J., Lebsock, M., Suzuki, K., Waliser, D., Wu, D., Kay, J., Gettelman, A., Wang, Z., and Marchand, R.: CloudSat mission: Performance and early science after the first year of operation, Journal of Geophysical Research Atmospheres, 114, https://doi.org/10.1029/2008JD009982, https://agupubs.onlinelibrary.wiley.com/doi/abs/10.1029/2008JD009982, 2009.

Tanelli, S., Durden, S. L., Im, E., Pak, K. S., Reinke, D. G., Partain, P., Haynes, J. M., and Marchand, R. T.: CloudSat's cloud profiling radar after two years in orbit: Performance, calibration, and processing, IEEE Transactions on Geoscience and Remote Sensing, 46, 3560–3573, https://doi.org/10.1109/TGRS.2008.2002030, http://ieeexplore.ieee.org/document/4685947/, 2008.

Ulaby, F. T., Moore, R. K., and Fung, K. A.: Microwave Remote Sensing, Addison-Wesley, 1981.

Wendisch, M., Brückner, M., Burrows, J., Crewell, S., Dethloff, K., Ebell, K., Lüpkes, C., Macke, A., Notholt, J., Quaas, J., Rinke, A., and Tegen, I.: Understanding Causes and Effects of Rapid Warming in the Arctic, Eos, https://doi.org/10.1029/2017eo064803, https://eos.org/project-updates/understanding-causes-and-effects-of-rapid-warming-in-the-arctic, 2017.

Wendisch, M., Macke, A., Ehrlich, A., Lüpkes, C., Mech, M., Chechin, D., Dethloff, K., Barientos, C., Bozem, H., Brückner, M., Clemen, H.-C., Crewell, S., Donth, T., Dupuy, R., Ebell, K., Egerer, U., Engelmann, R., Engler, C., Eppers, O., Gehrmann, M., Gong, X., Gottschalk, M., Gourbeyre, C., Griesche, H., Hartmann, J., Hartmann, M., Heinold, B., Herber, A., Herrmann, H., Heygster, G., Hoor, P., Jafariserajehlou, S., Jäkel, E., Järvinen, E., Jourdan, O., Kästner, U., Kecorius, S., Knudsen, E. M., Köllner, F., Kretzschmar, J., Lelli, L., Leroy, D., Maturilli, M., Mei, L., Mertes, S., Mioche, G., Neuber, R., Nicolaus, M., Nomokonova, T., Notholt, J., Palm, M., van Pinxteren, M., Quaas, J., Richter, P., Ruiz-Donoso, E., Schäfer, M., Schmieder, K., Schnaiter, M., Schneider, J., Schwarzenböck, A., Seifert, P., Shupe, M. D., Siebert, H., Spreen, G., Stapf, J., Stratmann, F., Vogl, T., Welti, A., Wex, H., Wiedensohler, A., Zanatta, M., and Zeppenfeld, S.: The Arctic Cloud Puzzle: Using ACLOUD/PASCAL Multi-Platform Observations to Unravel the Role of Clouds and

Aerosol Particles in Arctic Amplification, Bulletin of the American Meteorological Society, https://doi.org/10.1175/bams-d-18-0072.1, https://journals.ametsoc.org/doi/abs/10.1175/BAMS-D-18-0072.1, 2018.

Wesche, C., Steinhage, D., and Nixdorf, U.: Polar aircraft Polar5 and Polar6 operated by the Alfred Wegener Institute, Journal of large-scale research facilities JLSRF, 2, 87, https://doi.org/10.17815/jlsrf-2-153, https://jlsrf.org/index.php/lsf/article/view/153, 2016.

Winker, D. M., Pelon, J. R., and McCormick, M. P.: The CALIPSO mission: spaceborne lidar for observation of aerosols and clouds, in: Lidar Remote Sensing for Industry and Environment Monitoring III, edited by Singh, U. N., Itabe, T., and Liu, Z., vol. 4893, p. 1, Hangzhou, China, https://doi.org/10.1117/12.466539, http://proceedings.spiedigitallibrary.org/proceeding.aspx?doi=10.1117/12.466539, 2003.

Young, G., Jones, H. M., Choularton, T. W., Crosier, J., Bower, K. N., Gallagher, M. W., Davies, R. S., Renfrew, I. A., Elvidge, A. D., Darbyshire, E., Marenco, F., Brown, P. R., Ricketts, H. M., Connolly, P. J., Lloyd, G., Williams, P. I., Allan, J. D., Taylor, J. W., Liu, D., and Flynn, M. J.: Observed microphysical changes in Arctic mixed-phase clouds when transitioning from sea ice to open ocean, Atmospheric Chemistry and Physics, 16, 13 945–13 967, https://doi.org/10.5194/acp-16-13945-2016, https://www.atmos-chem-phys.net/16/13945/2016/, 2016.

Yuter, S. E. and Houze, R. A.: Three-Dimensional Kinematic and Microphysical Evolution of Florida Cumulonimbus. Part III: Vertical Mass Transport, Maw Divergence, and Synthesis, Monthly Weather Review, 123, 1964–1983, https://doi.org/10.1175/1520-0493(1995)123<1964:tdkame>2.0.co;2, https://journals.ametsoc.org/doi/abs/10.1175/1520-0493{%}281995{%}29123{%}3C1964{%}3ATDKAME{%}3E2.0.CO{%}3B2, 2002.

Table 11. Chirp settings and corresponding range resolution for the different research flights (RF). MiRAC has been operated on 19 RF.

	I	II	III
Period	RF04, RF05	RF19, 12:27 - 15:03 UTC RF22, 12:53 - 13:47 UTC	rest of RF
percentage of occurrence [%]	13	5	82
range gate resolution first chirp [m]	17.9	13.5	4.5
number of range gates first chirp	28	59	111
extent of first chirp [m]	500	800	500
range gate resolution second chirp [m]	27.0	22.4	13.5
number of range gates second chirp	126	183	253
extent of second chirp [m]	3400	4100	3400

Table 12. Specifications of MiRAC-P.

~~channel~~ frequency [GHz]	bandwidth [MHz]	T_R [K]	HPBW [deg]	gain [dB]
~~1~~183.31 $\pm$0.6	200	1350	1.3	41.2
~~2~~183.31 $\pm$1.5	200	1350	1.3	41.2
~~3~~183.31 $\pm$2.5	200	1550	1.3	41.2
~~4~~183.31 $\pm$3.5	400	1300	1.3	41.2
~~5~~183.31 $\pm$5.0	600	1300	1.3	41.2
~~6~~183.31 $\pm$7.5	1000	1400	1.3	41.2
~~7~~243	4000	900	1.25	43.6
~~8~~340	4000	2100	1.0	45.4

Table 13. Processing steps for MiRAC-A radar measurements

step	description	illustration in Fig. (5)
I	removal of mirror image	a) to b)
II	speckle filter	b) to c)
III	conversion from range to altitude system	c) to d)
IV	correction for sensor mounting and actual aircraft position	d) to e)
V	remapping onto constant vertical grid	e) to f)

Table 14. Positions and orientations of the reference frames. The x- and y-axes of X_g are defined in the common way: x_g points towards the intersection of the equator and the prime meridian and the y_g in the direction that completes the right-handed perpendicular coordinate system. Note that X_c is *not* located on the planet's surface but on the platform.

symbol	name	origin	x-axis	y-axis	z-axis	common coordinate name(s)
X_s	sensor-relative	payload sensor	*arbitrary*	sensor direction	*arbitrary*	range
X_p	platform-relative	platform	right wing	nose	stabilizer	right, forward, upward
X_c	local Earth-relative	platform	east	north	zenith	east, north, zenith
X_g	global geographic	Earth's center	*see caption*	*see caption*	North Pole	longitude, latitude, altitude

Table 15. Properties of clouds detected above ocean, sea ice and both surface types.

	ocean	ice	all
percentage of surface type[%]	56.5	43.5	100
cloud fraction [%]	80.1	72.0	75.5
precipitation fraction [%]	36.0	37.9	37.1
median CTH [m]	1350	1260	1305
mean CTH [m]	1768	1683	1722
percentage of 1 layer clouds [%]	65.3	60.0	62.4
percentage of 2 layer clouds [%]	33.2	36.0	34.7
percentage of $\geq$ 3 layers clouds [%]	1.5	4.0	2.7

Table 16. Filter names and quality control of data in PANGAEA-files (Kliesch and Mech, 2019), description to variable "Ze flag", row 1 to 4 is already applied to get from "Ze unfiltered" to "Ze" and row 5 to 8 help for analyzing teh data.

flag name	description
defective gate filter	increased reflectivity values in specific range gates are removed by a threshold
snr filter	anything below Z_{min} is removed
speckle filter	side-lobe disturbances and speckle are removed
subsurface reflection filter	side-lobe disturbances are removed
quality disturbance possible range	possible range of side-lobes
quality surface influence range	range of surface contamination
quality disturbance in cloud	side-lobe disturbance in cloud (manually added)
quality disturbance	disturbance (manually added)